Published in final edited form as:
Nature. 2016 September 01; 537(7618): 107–111. doi:10.1038/nature19326.

An endosomal tether undergoes an entropic collapse to bring vesicles together

David H. Murray[#1], **Marcus Jahnel**[#1,2,3], **Janelle Lauer**[1], **Mario J. Avellaneda**[1,2,5], **Nicolas Brouilly**[1], **Alice Cezanne**[1], **Hernán Morales-Navarrete**[1], **Enrico D. Perini**[1,2], **Charles Ferguson**[6], **Andrei N. Lupas**[4], **Yannis Kalaidzidis**[1], **Robert G. Parton**[6,7], **Stephan W. Grill**[1,2,3,$], and **Marino Zerial**[1,$]

[1]Max Planck Institute of Molecular Cell Biology and Genetics, Pfotenhauerstrasse 108, 01307 Dresden, Germany

[2]Biotechnology Center, Technical University Dresden, Tatzberg 47/49, 01307 Dresden, Germany

[3]Max Planck Institute for the Physics of Complex Systems, Nöthnitzerstraße 38, 01187 Dresden, Germany

[4]Department of Protein Evolution, Max-Planck-Institute for Developmental Biology, 72076 Tübingen, Germany

[6]Institute for Molecular Bioscience, The University of Queensland, St Lucia 4072, Australia

[7]Centre for Microscopy and Microanalysis, The University of Queensland, St Lucia 4072, Australia

[#] These authors contributed equally to this work.

Abstract

An early step in intracellular transport is the selective recognition of a vesicle by its appropriate target membrane, a process regulated by Rab GTPases via the recruitment of tethering effectors1–4. Membrane tethering confers higher selectivity and efficiency to membrane fusion than the pairing of SNAREs alone5,6,7. Here, we addressed the mechanism whereby a tethered vesicle comes closer towards its target membrane for fusion by reconstituting an endosomal asymmetric tethering machinery consisting of the dimeric coiled-coil protein EEA16,7 recruited to phosphatidylinositol 3-phosphate membranes and binding vesicles harboring Rab5. Surprisingly, structural analysis revealed that Rab5:GTP induces an allosteric conformational change in EEA1,

[$]Correspondence: Stephan Grill (stephan.grill@biotec.tu-dresden.de) and Marino Zerial (Zerial@MPI-CBG.de).
[5]Present address: FOM Institute AMOLF, Science Park 104, 1098 XG Amsterdam, Netherlands

Author Contributions

D.H.M., M.J., S.W.G. and M.Z. conceived the project together. D.H.M. prepared all reagents, performed experiments and their analysis. M.J. und S.W.G. interpreted data in the context of polymer physics. M.J. performed optical tweezer experiments with D.H.M. M.J.A. and E.P. performed initial tweezer experiments. M.J. and M.J.A. analysed tweezer experiments. D.H.M., J.L. and A.N.L. designed mutants. N.B. performed super-resolution experiments. A.C. assisted in reconstitution experiments. C.F. and R.G.P. performed cell electron microscopy, and D.H.M., H.M.-N. and M.J. analysed electron microscopy data. Y.K. analysed cell microscopy. D.H.M., M.J., S.W.G. and M.Z. wrote the manuscript with input from all the authors.

Competing financial interests

The authors declare no competing financial interests.

Europe PMC Funders Author Manuscripts

from extended to flexible and collapsed. Through dynamic analysis by optical tweezers we confirmed that EEA1 captures a vesicle at a distance corresponding to its extended conformation, and directly measured its flexibility and the forces induced during the tethering reaction. Expression of engineered EEA1 variants defective in the conformational change induced prominent clusters of tethered vesicles *in vivo*. Our results suggest a new mechanism in which Rab5 induces a change in flexibility of EEA1, generating an *entropic collapse force* that pulls the captured vesicle toward the target membrane to initiate docking and fusion.

EEA1, as nearly all putative coiled-coil tethering proteins, extends more than 10 times the length of SNARE proteins8,9. To explain how such a long molecule can mediate membrane tethering but also permit the membranes to come closer for fusion we reconstituted a minimal asymmetric membrane tethering in liposomes containing EEA1, Rab5 and different fluorescent tracers (Fig. 1a; Extended Data Fig. 1b-e). EEA1 binds to PI(3)P via its C-terminus with high affinity (K_d~50 nM)7,10–12, and to Rab5:GTP via its N-terminus with comparatively lower affinity (K_d~2.4 μM)13. Liposomes containing PI(3)P and labeled with RhoDPPE effectively recruited EEA1 and tethered to DiD-labeled Rab5-6xHis-liposomes, as analyzed by confocal microscopy (Fig. 1a-c). The reaction required EEA1, Rab5 and GTPγS, as no colocalization was observed in the presence of GDP. The efficiency of tethering approached that of biotin-streptavidin liposomes (Fig. 1d). Furthermore, no colocalization was observed between pairs of liposomes harboring Rab5 (Fig. 1e). Therefore, Rab5, EEA1 and PI(3)P form a minimal endosomal asymmetric membrane tethering machinery.

In principle, the N-terminus of EEA1 could also bind Rab5 in *cis*, i.e. on the same membrane. However, the presence of Rab5 on both pairs of liposomes, as in early endosomes *in vivo*, did not interfere with the tethering activity of EEA1 *in vitro*, as tethering was indistinguishable between the asymmetric and symmetric conditions (Fig.1c,e). Moreover, coiled-coil prediction algorithms estimate a central segment of nearly ~200 nm14,15 (Extended Data Fig. 1a), suggesting that the molecule adopts an extended conformation. Indeed, filamentous EEA1-positive structures emanating from the surface of early endosomes *in vivo* have been observed by EM11. In further support of this interpretation, we visualized the N- and C- termini of EEA1 using specific antibodies by super-resolution microscopy in HeLa cells (Fig. 1f,g, Extended Data Fig. 1f-h, Methods). If the N-terminus of EEA1 bound Rab5 in *cis*, it should colocalize with the C-terminus. Strikingly, the ends of EEA1 could instead be resolved, with the N-terminus extending radially from the C-terminus into the cytoplasm. We estimated an end-to-end of distance of 141±47 nm (mean±SD; Fig. 1h), in the range of the predicted length and rigidity of coiled-coils.

To characterize the distances and dynamics of the tethering reaction, we generated bead-supported membranes (10 μm silica microspheres) harboring GFP-Rab5 (Fig. 1i, Extended Data Fig. 2). These tethered to liposomes containing PI(3)P in the presence of GTPγS but not GDP in an EEA1 concentration-dependent manner (Extended Data Fig. 2g,h). Time-lapse microscopy showed that some liposomes were captured by the bead-supported membrane, while others diffused away (Extended Data Fig. 2i, Video 1,2), similar to the

behavior of endosomes *in vivo*16. We next measured the distances between the tethered vesicle and GFP-Rab5 (Fig. 1j, Extended Data Fig. 2j, Methods). Surprisingly, we observed distances ranging from 20 nm up to approximately the predicted length of 200 nm (mean ±SD; 84±56 nm) (Fig. 1k). Such a broad distribution is irreconcilable with the predicted length of EEA1 and suggests that EEA1 may change its conformation.

We determined the conformation of EEA1 using rotary shadowing EM and image analysis (Fig. 2a). The measurements of contour length and mean end-to-end distance follow Gaussian distributions with an average of 222±26nm (Fig. 2b, top panel) and 195±26nm (Fig. 2b, bottom panel), respectively, confirming that the molecule is largely extended, as *in vivo*11 (Fig. 1g,h). However, this is incompatible with the much shorter distances between tethered vesicles *in vitro* (Fig. 1k). Therefore, we asked whether binding to Rab5 may cause EEA1 to adopt a more compact conformation. Remarkably, this was the case. Addition of Rab5:GTPγS (Fig. 2c) resulted in a significant fraction of bent EEA1 molecules having a substantially reduced end-to-end distance of 122±50nm (Fig. 2d).

To gain further insights into this mechanism, we generated two mutants with alterations in the coiled-coil but retaining the Rab5- and PI(3)P-binding domains (Extended Data Fig. 3, Methods). In the extended EEA1 mutant, we removed regions of discontinuity between heptad repeats creating a more idealized, extended coiled-coil. In the swapped EEA1 mutant, we swapped the coiled-coil regions between the N- and C-termini. EM analysis revealed that the extended mutant was impaired in the Rab5-induced conformational change (Fig. 2i, Extended Data Fig. 4a-c). In contrast, the swapped mutant was mostly bent, often presented kinks, and did not significantly change conformation upon Rab5 binding (Fig. 2f, Extended Data Fig. 4e-g). These results suggest that coiled-coil discontinuities and their physical arrangement are critical for the structure of EEA1 and its Rab5-induced conformational change.

To shed light on how EEA1 adopts a compact conformation upon Rab5 binding, we measured the curvature along the contour of molecules. We aligned N-terminally MBP-tagged EEA1 and determined how the tangents to the contour change by 8 nm steps along the contour (Methods, Extended Data Fig. 5). Interestingly, the variance of this measure of curvature calculated over the ensemble of molecules increased significantly upon Rab5:GTPγS binding (Fig. 2g), indicating that EEA1 displays a larger variety of curvatures upon Rab5:GTP binding. Such changes occurred along the entire length of the molecule, with some regions increasing in flexibility more than others (Fig. 2g), but were not observed for the EEA1 mutants (Extended Data Fig. 5f-i).

Although molecules are adsorbed onto a 2D surface, some aspects of their 3D conformations are captured (Methods). Analysis of the kurtosis of the distribution of angles between contour tangents indicated that 3D shape fluctuations are retained for the entire contour of EEA1 in the presence of Rab5:GDP, but only up to 60 nm with Rab5:GTPγS (Methods, Extended Data Fig. 6). Moreover, tangent-tangent correlations of the contour in this regime revealed that Rab5:GTPγS binding results in a faster decay. Generally, the worm like chain (WLC) model is used to describe fluctuations in polymer shapes and capture aspects of the physics underlying their shape fluctuations17 (Methods). In the WLC model, the polymer is

considered a homogeneous molecule with its flexibility determined by a bending stiffness reflected in a characteristic length, i.e. the persistence length, over which correlations between tangents to the contour decay. We applied the WLC model to EEA1 and determined an effective persistence length of 246±42 nm for the unbound and 74±3 nm for the Rab5:GTPγS-bound ensembles. In contrast, the extended EEA1 mutant had similar effective persistence lengths in either state (unbound=183±13 and bound=224±25 nm, Table 1).

To corroborate these estimates, we fit the radial distribution functions (i.e. the probability of observing a given end-to-end distance) of the molecules extracted from the EM data with analytical solutions of the WLC model18 (Methods). This showed a clear reduction in effective persistence length of EEA1 upon Rab5:GTP binding (Fig. 2h). In contrast, the extended EEA1 mutant maintained a similar radial distribution regardless of Rab5 (Extended Data Fig. 4d).

Reducing the persistence length of EEA1 makes the molecule flexible. However, the tether is still extended and therefore, in an out-of-equilibrium conformation (Fig. 2e). As a result, it will undergo an entropic collapse, with its end-to-end distance decreasing towards a new equilibrium (Fig. 2f). This process generates a force that could pull the membranes together (estimated ~3 pN (Methods). In some sense, the extended molecule is like a loaded spring that rapidly recoils upon Rab5 binding.

To provide experimental evidence for entropic collapse of EEA1, we made use of high-resolution dual-trap optical tweezers (Methods). Two glass 2 μm microspheres coated with membranes were held in optical traps (Fig. 3a). One trap was moved closer to the other, in iterative cycles of approaching, pausing and retracting (Fig. 3b). At distances below 250 nm and at low concentrations of EEA1 (5-40 nM) to ensure single molecule events, we observed transient interactions as a decrease in mean and variance of the distance between the two beads (Fig. 3b, red arrows; Fig. 3c; Extended Data Fig. 7a,d). Interactions were infrequent, as expected for single molecules and non-existent without EEA1, whereas their frequency and duration increased at high concentrations of EEA1 (400 nM) (Extended Data Fig. 7e, Methods). The interaction distance was broad (Fig. 3d) with the mean 176±76 nm comparing favorably to rigid EEA1 (Fig. 2b).

To test the prediction that EEA1 becomes flexible upon Rab5 binding, for each tethered molecule we determined its effective persistence length from the capture distance, measured force increase (Fig. 3c), and bead displacements using the WLC model (Methods). Strikingly, we obtained a median effective persistence length of 23±10 nm (Fig. 3e). For >80% of the molecules the persistence length was ≤1/2 of the contour length, confirming that Rab5-bound EEA1 is flexible. In contrast, the extended EEA1 mutant remained significantly more rigid than EEA1 (Fig. 3e). Rab5 binding is necessary to trigger structural and conformational changes on EEA1. When Rab5 was bypassed by His-tag mediated tethering, EEA1 flexibility was significantly lower than that of EEA1 with Rab5 (Fig. 3e).

If EEA1 becomes flexible upon capture, an entropic pulling force will be generated. This entropic force balances with the force exerted by the optical traps as the molecule undergoes the collapse and as the system finds its new equilibrium (Extended Data Fig. 7h)19. For a

capture distance of 195 nm and a peak collapse force of 3 pN, we predict a force balance at ~0.6pN (Methods), consistent with our tweezer measurements of 0.5±0.3 pN (Fig. 3c). EEA1 binding to Rab5 requires the GTP-bound form. No significant force differences were observed in the presence of the non-hydrolysable analogue GTPγS or GTP (Fig. 3f). In contrast, the duration of the interaction was much prolonged (Fig. 3g), as expected given that GTPγS stabilizes Rab5 in the active form20. Finally, replacing EEA1-Rab5 binding with 10xHis-EEA1 tethering to Ni-NTA-beads resulted in a decreased collapse force (Extended Data Fig. 7i).

To validate *in vivo* the mechanism observed *in vitro*, we genome-edited HeLa cells to disrupt the EEA1 gene (HeLa EEA1-KO, Fig. 4a, Extended Data Fig. 8c, Methods), and analyzed the distribution of Rab5-positive endosomes and the uptake of cargo (LDL) by confocal microscopy (Fig. 4a). HeLa EEA1-KO displayed a significant reduction in Rab5 endosome size, particularly for the largest endosomes (Fig. 4c), and a marked decrease in cargo (LDL) uptake (Fig. 4f). Expression of EEA1 rescued the normal, rounded morphology of endosomes (Fig. 4b, Extended Data Fig. 8f,i) and LDL uptake (Fig. 4c). In contrast, the expression of both extended and swapped EEA1 mutants generated enlarged endosomes and inhibited cargo uptake (Fig. 4c-f).

Because the size of endosomes is below the resolution limit of light microscopy, we performed EM on the HeLa EEA1-KO cells (Fig. 5, Extended Data Fig. 9). The filamentous material on endosomes11 was much reduced in HeLa EEA1-KO cells (Fig. 5a,b, and Extended Data Fig. 8n) and restored by the re-expression of EEA1 on endosomes that appeared normal or enlarged, consistent with the light microscopy analysis (Fig. 4b). Strikingly, cells expressing the extended EEA1 mutant had large (>1 μm) clusters of small vesicles, within areas filled with filamentous material (Fig. 5d,e), suggesting that they are arrested in a tethered state (Fig. 4d-e). The distance between the tethered vesicles was significantly longer than that between endosomes in control cells (Extended Data Fig. 8o), consistent with the mutant EEA1 being incapable of undergoing entropic collapse to shorter distances (Fig. 2e, 3e). Similar endosomal clusters were induced by the swapped mutant (Extended Data Fig. 8m).

Our data suggest a new mechanochemical cycle of EEA1 regulated by Rab5:GTP binding and GTP hydrolysis. On early endosomes, EEA1 is in the extended state (Fig. 2e) and increases the probability of capturing a vesicle bearing Rab5. Similarly, it forms a Rab5-selectivity barrier (analogous to a polymer brush)21. When Rab5 on an incoming vesicle binds EEA1, it induces an allosteric conformational change, from extended to flexible (Fig. 2f). This shows a new function of Rab proteins beyond effector recruitment. The reduction in persistence length of EEA1 causes its entropic collapse, releasing up to ~14 k_BT of mechanical energy (Extended Data Fig. 7k) and generating up to 3 pN of force that could pull the vesicle closer to its target membrane where it may diffuse22 or be brought by other Rab5 effectors23,24 within the range of trans-SNARE pairing. This mechanism explains why the Rab5 machinery dramatically increases the efficiency of SNARE-mediated membrane fusion23. The mechanical energy released by EEA1 is on the order of the free energy released by GTP hydrolysis. However, the energy required to complete the cycle could potentially also come from chaperones.

A key question is how Rab5 can induce such a long-range allosteric effect. This is not uncommon among coiled-coil proteins25,26. The entropic collapse mechanism is different however for other membrane tethering factors27. In the course of this study, the GCC185 tether was shown to bend through central joints27. For EEA1, instead, 1) the arrangement and structure of the coiled-coils, and 2) Rab5 binding are critical for the propagation of allosteric conformational changes (Extended Data Fig. 10). We can envisage different mechanisms (see Supplementary Discussion), such as local register shifts. In dynein, dynamics in the heptad register prove critical to functionally link ATP binding and microtubule binding at opposite ends of its coiled-coil stalk28,29. Further *ad hoc* structural studies are necessary to resolve this outstanding problem. The entropic collapse upon stiffness reduction could be an effective and general mechanism used not only by membrane tethers but also by many coiled-coil proteins for generating an attractive force in diverse biological processes.

Methods

Statistics

Sample size was not predetermined. Box-whiskers plots all show median, 25/75 quartiles by box boundaries, and min/max values by errors with exception of Fig. 3 and Extended Data Fig. 7 which use Tukey–defined error bars.

Cloning, expression, and purification of proteins

Human Rab5-6xHis and GFP-Rab5-6xHis were expressed and purified essentially as previously described in the *E. coli* expression system6. Human Rabex-5 amino acid residues 131-394 were PCR and restriction cloned into a pGST-parallel2 vector containing a TEV cleavable N-terminal glutathione-S-transferase (GST)29, 30. Expression and purification was performed essentially as described31. Briefly, *E. coli* expressed proteins were transformed into BL21(DE3) cells and grown at 37°C until an OD600=0.8, whereupon the incubator was reduced to 18°C. After 30 minutes, cultures were induced with 0.1 mM IPTG and grown overnight (16 hours). Cell pellets were resuspended in standard buffer (20 mM Tris pH7.4, 150 mM NaCl, 0.5 mM TCEP) and flash frozen in liquid nitrogen. All subsequent steps performed at 4°C or on ice. Cell pellets were resuspended in standard buffer supplemented with 1 mM MgCl2 for GTPases, and protease inhibitor cocktail (chymostatin 6 μg/mL, leupeptin 0.5 μg/mL, antipain-HCl 10 μg/mL, aprotinin 2 μg/mL, pepstatin 0.7 μg/mL, APMSF 10 μg/mL), homogenized and lysed by sonication. Histidine-tagged proteins were bound in batch to Ni-NTA resin in the presence of 20 mM imidazole, and eluted with 200 mM imidazole. GST tagged proteins were purified on GS resin (GS-4B, GE Healthcare) by 2 hour binding followed by stringent washing, and cleavage from resin overnight. Imidazole-containing samples were immediately diluted after elution and tags cleaved during overnight dialysis. Following dialysis and tag cleavage, samples were concentrated and TEV or HRV 3C protease was removed by reverse purification through Ni-NTA or GS resin. Samples were then purified by size-exclusion chromatography on Superdex 200 columns in standard buffer.

Human EEA1 was purified as a GST fusion in a pOEM series vector (Oxford Expression Technologies) modified to contain a HRV 3C-cleavable N-terminal GST and protease cleavage site or from a modified pFastbac1 vector (Thermo Fisher Scientific)23. Some samples were also purified as 6xHis-MBP and 10xHis fusions from a modified pOEM vector (rotary shadowing for N-to-C terminus alignment, and optical tweezer control, respectively; all other experiments performed with tags removed). Mutants were purified identically to wild-type EEA1.

SF9 cells growing in ESF921 media (Expression Systems) were co-transfected with linearized viral genome and the expression plasmid and selected for high infectivity. P1 and P2 virus was generated per manufacturer's protocol, and expression screens and time-courses performed to optimize expression yield. Best viruses were used to infect 1-2 L SF9 cells at 10^6 cells/mL at 1% vol/vol and routinely harvested after 40-48 hours at about $1.5x10^6$ cells/mL, suspended in standard buffer, and flash frozen in liquid nitrogen. Pellets were thawed on ice and lysed by Dounce homogenizer. Purification took place rapidly in standard buffer at 4°C on GS resin in batch format. Bound protein was washed thoroughly and cleaved from resin by HRV 3C protease overnight. Proteins retaining 6xHis-MBP tags were purified on amylose resin and eluted with 10 mM maltose. Protein retaining 10xHis were eluted from Ni-NTA resin in standard buffer supplemented with 200 mM imidazole. All EEA1 and mutants were immediately further purified by Superose 6 size-exclusion chromatography where they eluted as a single peak. All experiments were performed with a preparation confirmed for Rab5 and PI(3)P binding. Concentrations were determined by UV280 and Bradford assay. All proteins were aliquoted and flash frozen in liquid nitrogen and stored at -80° C.

EEA1 variants extended and swapped were synthesized genes optimized for insect cell expression (Genscript). The extended mutant has regions of low coiled-coil prediction removed, resulting in an EEA1 construct 1286 amino acids in length (versus 1411 in wild-type EEA1) (see Extended Data Fig. 3). The swapped mutant has the C-terminal portion of the coiled-coil rearranged to follow the N-terminal Zn^{2+}-finger domains, and the N-terminal portion of the coiled-coil therefore rearranged to the C-terminal region of EEA1. Variants were treated identically to wild-type EEA1 in purification.

Static light scattering

An autosampler equipped Viskotek TDAMax system was used to analyze the light-scattering from purified EEA1. Sample was loaded the autosampler and passed through a TSKGel G5000PW column (Tosoh Biosciences) and fractions were subjected to scattering data acquisition. Data obtained were averaged across the protein elution volume and molecular weights determined in OmniSEC software package.

Lipids

The following lipids were purchased and used directly: DOPC, DOPS, DOGS-NiNTA, RhoDPPE (Avanti), DiD (Invitrogen), and PI(3)P (Echelon Biosciences). Lipids were dissolved in chloroform, except PI(3)P in 1:2:0.8 $CHCl_3$:MeOH:H_2O. All were stored at -80 °C.

Rab5/PI(3)P binding by EEA1

Early endosome fusion assay was performed as previously described32. To assess the ability of EEA1 to bind competently in a GTP-dependent manner to Rab5, Rab5 was bound to GS resin and subsequently loaded with nucleotide (GDP, GTPγS) as previously described6. Binding of EEA1 and all variants to immobilized Rab5 proceeded for one hour at room temperature, and the washed Rab5 resin was evaluated for EEA1 binding by Western blot. Similarly, the binding of EEA1 to PI(3)P containing liposomes was evaluated as previously described by formation of liposomes composed of DOPC:DOPS or DOPC:DOPS:PI(3)P (85:15 or 80:15:5 respectively)33. Briefly, liposomes were formed from the hydration of lipids at 1 mM in standard buffer, and combined with EEA1 for 1 hour before ultracentrifugation to separate supernatant and pellet for Western blotting to evaluate EEA1 sedimentation. Rabbit anti-EEA1 antibody was made in our lab.

Preparation of liposomes

Liposomes were formed by extrusion as previously described34. Liposome compositions for fluorescence microscopy tethering assays were: DOPC:DOPS:DOGS-NiNTA, DOPC:DOPS:PI(3)P, DOPC:DOPS:biotin-DPPE, with RhoDPPE and DiD where applicable. Liposome compositions for bead-supported membranes were DOPC:DOPS:DOGS-NiNTA, DOPC:DOPS:PI(3)P. Solvent was evaporated under nitrogen and vacuum overnight. The resulting residue was suspended in standard buffer, rapidly vortexed, freeze-thawed five times by submersion in liquid N2 followed by water at 40 °C, and extruded by 11 passes through two polycarbonate membranes with a pore diameter of 100 nm (Avestin). Vesicles stored at 4°C were used within 5 days.

Bead-supported bilayer preparation

Silica beads (2 μm NIST-traceable size-standards for optical tweezers, or 10 μm standard microspheres for microscopy; Corpuscular) were thoroughly cleaned in pure ethanol and Hellmanex (1% sol., Hellma Analytics) before storage in water. Supported bilayers were formed as previously described with modifications35. Liposomes composed of DOPC:DOPS 85:15 (with 5% PI(3)P and DOGS-NiNTA where applicable) were added to a solution containing 250 mM NaCl for tethering assays (10 μm) and 100 mM for optical tweezers (2 μm), and $5x10^6$ beads. Liposomes were added to final concentration of 100 μM and incubated for 30 minutes (final volume 100 μL). Samples were washed with 20 mM Tris pH7.4 three times by addition of 1 mL followed by gentle centrifugation (380 x g). Final wash was with standard buffer. Salt concentrations were optimized by examination of homogeneity at the transverse plane followed by examination of the excess membrane at the coverslip plane (see Extended Data Fig. 2a-d). We found that the membranes were extremely robust in conditions where the bilayer is fully formed, and could be readily pipetted and washed, consistent with previous reports36. Membrane-coated beads were used within 1 hour of production and always stored prior to use on a rotary suspension mixer.

Confocal microscopy of vesicle-vesicle tethering assay

Glass coverslips were cleaned in ethanol, Hellmanex, and thoroughly rinsed in water. In these experiments, the following concentrations were used: 1 nM Rabex-5(131-394), 100

nM Rab5-6xHis, 120 nM EEA1. Experiments were performed in standard buffer with 5 mM MgCl2 and 1 μM nucleotide. Liposomes and proteins were pre-mixed in low-binding tubes at concentrations indicated, incubated for five minutes, and imaged immediately upon addition to the coverslip. Images were acquired with a Nikon TiE equipped with a 60x plan-apochromat 1.2NA W objective and Yokagawa CSU-X1 scan head. Images were acquired on an Andor DU-897 back-illuminated CCD. Acquired images were processed by the SQUASH package for Fiji37.

Confocal microscopy of bead-supported membrane tethering assay

A 200 μL observation chamber (u-Slide 8 well, uncoated, #1.5, ibidi) was pre-blocked with BSA (1 mg/mL in standard buffer) for 1.5-2 hours and washed thoroughly. Finally, 180 μL of standard buffer containing beads was added to the sample chamber. In these experiments, the following concentrations were used: 1 nM Rabex-5(131-394), 100 nM GFP-Rab5-6xHis, and the given EEA1 concentrations (between 30 and 400 nM). Nucleotide control experiments were performed at 190 nM EEA1. Experiments were performed in standard buffer with 2 mM MgCl2 and 1 mM nucleotide. Altogether Rab5, Rabex5, nucleotide, EEA1, and buffer were mixed in low-binding tubes at concentrations indicated, and were added to 240 μL final volume to assure mixing throughout the chamber volume.

Images for colocalization analysis were acquired with a Nikon TiE equipped with a 60x plan-apochromat 1.2NA W objective and Yokagawa CSU-X1 scan head. Images were acquired on an Andor DU-897 back-illuminated CCD. Acquired images were processed by the SQUASH package for Fiji37.

Data obtained for distance measurements was acquired in the same way and processed in Fiji by determining line profiles 8 pixels wide from the center of the bead outwards over an observed vesicle. These profiles were fit with a Gaussian distribution. The alignment of the microscope was confirmed by imaging of sub-diffraction beads, revealing no clear systematic shift and a maximum positional error of 21 nm determined in Motion Tracking16. Controls with sub-diffraction-sized multicolor particles (Methods) and distance measurements between Rab5 itself and its resident membrane were within the measurement error of the technique (approximately 15 nm)38.

Super-resolution imaging of EEA1 termini

HeLa cells were stained using primary antibodies against EEA1 N-terminus (610457, prepared in mouse, BD Biosciences) and EEA1 C-terminus (2900, prepared in rabbit, Abcam). The secondary antibodies were anti-mouse Alexa568 antibody (A-11004, prepared in goat, Life Technologies) and anti-rabbit Alexa647 (A-21244, prepared in goat, Life Technologies). Coverslips were mounted in STORM buffer (100mM Tris-HCl pH8.7, 10mM NaCl, 10% glucose, 15% glycerol, 0.5mg/ml glucose oxidase, 40ug/ml catalase, 1% BME) and sealed with nail polish. Cells were imaged on a Zeiss Eclipse Ti microscope equipped with a 150mW 561nm laser and a 300mW 647 laser. For imaging, lasers intensities were set to achieve 50mW at the rear lens of the objective. Illumination was applied at a sub-TIRF angle through the objective to improve the signal to noise ratio. Videos of 24000 frames (12000 frames per channel) were acquired by groups of 6 consecutive frames using the NIS

Elements software (Nikon). Images were aligned using 100 nm Tetraspeck beads (Thermo Fisher). This software was also used for peak detection and image reconstruction. The localization of the EEA1 termini could be distorted a maximum of approximately 20 nm due to the size of the antibodies. The localization accuracy of the secondary antibody was ~25 nm. Measured distances were determined in Fiji and represent distances between respective centers-of-mass. Representative experiment is shown, n=3.

Sample preparation for optical trap experiments

Bead-supported membranes were prepared as described. The concentrations used were as in the microscopy experiments: 1 nM Rabex-5(131-394), 100 nM Rab5-6xHis, and EEA1 concentrations (between 30 and 400 nM). Most experiments were performed at 40 nM EEA1, with additional trials taking place at 4 and 400 nM. At lowest concentrations, single transient events became difficult to observe (<5% had interactions). At the highest concentrations, events were often non-transient or repeated.

Electron microscopy

Samples were rotary-shadowed essentially as described39. Briefly, samples were diluted in a spraying buffer, consisting of 100mM Ammonium acetate and 30% Glycerol. Diluted samples are sprayed via a capillary onto freshly cleaved mica chips. These mica chips are mounted in the high vacuum evaporator (MED 020, Baltec) and dried. Specimens are platinum coated (5-7.5 nm) and carbon is evaporated. Following deposition, the replica was floated off and examined at 71,000x magnification and imaged onto a CCD (Morgagni 268D, FEI; Morada G2, Olympus).

Analysis of electron microscopy

Images obtained were processed in ImageJ by skeletonizing the particles. Lengths were determined directly from this data and represent an overestimation due to the granularity of the platinum shadowing (5-7.5 nm granules). The bouquet plots were generated by aligning the initial five segments of the molecules and the entire population set was plotted.

To determine the curvature measure, we first took the skeletonized curves and smoothed them with a window of 8.2 nm. These curves were then segmented with 301 equally spaced points, and these smoothed curves were used for the curvature calculation. We first attempted to define curvature at 1 segment length (~0.75 nm) but this analysis was too noisy to obtain meaningful description of the curves. We therefore determined the curvature by taking the difference of the tangents and diving it by the arc length at a distance of ~15 nm (20 points). The variance of this measure was determined, and bootstrapping with resampling was used to determine errors over the whole population and for 1000 iterations.

Although proteins are not homogeneous polymers, the WLC model captures essential aspects of the physics underlying their shape fluctuations40,41. Calculation of fits to all mean tangent-correlations and the equilibration analysis, were performed using Easyworm source code in Matlab42. First, the original skeletonized curves were segmented with 301 equally spaced points. This data was then used to calculate the tangent-correlations and the kurtosis plots. We fitted the regime whereby the kurtosis measurement defined that the

molecules were equilibrated18,43,44. This distance therefore varied (see Extended Data Fig. 6, kurtosis plots), but the estimation of persistence length was only weakly dependent on this distance. The fitting routines were then implemented up to the thermal equilibration distance with bootstrapping with resampling, which was run for the whole population and 1000 times to obtain errors. These are given as mean±standard deviation. For values and fit statistics, please refer to Table 1. We did not apply the WLC model to the swapped mutant (Extended Data Fig. 4h) due to the lack of significant structural changes upon Rab5 binding (Fig. 2f, Extended Data Fig. 4f).

The analytical fit to the radial distribution functions were performed in Python18. The radial distribution function for a worm-like chain is the probability density for finding the end points of the polymer. The polymers are considered as embedded in a two-dimensional space in this scheme. This treatment adopts the continuum model of the polymer, thereby defining the statistical properties via free energy calculation. Fit to analytical solution of the WLC yielded a mean effective persistence length of 270±14 nm for EEA1 alone (mean ±error of fit), and two populations of effective persistence lengths (26±2 nm [67%] and 300±14 nm [33%]) for EEA1 in the presence of Rab5:GTPγS.

Optical tweezer experiments

A custom-built high-resolution dual-trap optical tweezer microscope was used45,46. A single stable solid-state laser (Spectra-Physics, 5W) is split by polarization into two traps that can be independently maneuvered. Forces were measured independently in both traps by back-focal plane interferometry. Absolute distances between the two traps were determined by template-based video microscopy analysis (43±2 nm px^{-1}) and offset-corrected for each microsphere pair by repeatedly contacting the microspheres after each experiment. The template detection algorithm has subpixel accurate, at an estimated uncertainty in absolute distance measurements to be not more than ±20 nm. Bead displacement was calculated according to $\Delta F = - \kappa \cdot \Delta y$. Extended Data Fig. 7g demonstrates the sensitivity of the instrument via the Allan deviation47 for averaging times greater than 100 ms.

All optical tweezer experiments were performed with 2 μm silica size-standard microspheres (Corpuscular), at a temperature of 26±2 C in a laminar flow chamber with buffers containing 35 % glycerol to prevent sedimentation of the silica microspheres. Thermal calibration of the optical traps was performed with the power spectrum method using a dynamic viscosity of 3.1 mPas48 (mean trap stiffness, trap 1: κ_1 = 0.035 ± 0.007 pN/nm, trap 2: κ_2 = 0.029 ± 0.007 pN/nm), leading to an overall trap stiffness of κ_T = 0.0159 pN/nm (yellow response curve in Extended Data Fig. 7h). Data was acquired at 1 kHz and further processed using custom written software in R. Spurious electronic noise at 50 Hz was filtered using a 5^{th}-order Butterworth notch filter from 49 to 51 Hz.

For probing the interactions of EEA1 with Rab5 without any assumptions on the shape of EEA1, a distance agnostic protocol with consecutive cycles of approaching, waiting (20 s) and retraction was used, approaching closer in each iteration (Fig. 3b). The stationary segments were then subjected to automatic changepoint analysis to identify regions of the time series longer than 100 ms with significantly different mean and variance49. Events thus

identified were classified as transient if the mean and variance went back to base levels within the stationary segment (see examples in force traces in Fig. 3c, Extended Data Fig. 7). Mean times of interactions were 3.4±0.6 s for GTPγS and 0.9±0.2 s for GTP. A fluctuation analysis of the differential distance signal during these events gave an estimated tether misalignment of less than 30° in all interactions. Only transient events were further processed50. Silica beads alone as a negative control measured a mean contact distance of 22 nm (Fig. 3d , grey).

To calculate the persistence length for individual captured molecules we determined the equilibrium extension, Z_{eq}, from the capture distance D [nm], the average measured force increase upon tethering ΔF [pN] and the known displacements from each trap $\Delta x_1 = \Delta F/\kappa_1$ and $\Delta x_2 = \Delta F/\kappa_2$ as $z_{eq} = D - \Delta x_1 - \Delta x_2$. With this distance, the persistence length was calculated according to51:

$$\lambda\left(\Delta F,\, z_{eq}\right) = \frac{k_B T}{\Delta F}\left(\frac{z_{eq}}{L} - \frac{1}{4} + \frac{1}{4\left(1 - z_{eq}/L\right)^2}\right)$$

Similarly, to estimate the magnitude of the entropic collapse force, this formula was applied to the equilibrium extensions of EEA1, as estimated by the end-to-end distances of the molecules from electron microscopy. Values determine were EEA1, 23 [14, 33] nm. Extended, 73 [60, 88] nm. Swapped, 26 [21, 30] nm. 10xHis, 78 [35, 140] nm, median and bounds at [2.5%, 97.5%]. Values reported are median and 95% confidence interval determined from bootstrapping

Generation of HeLa EEA1-KO cell line

HeLa EEA1-KO lines were generated using CRISPR-Cas9 technology52 on HeLa-Kyoto cell lines obtained from the BAC recombineering facility at MPI-CBG. Cell lines were tested for mycoplasma, and authenticated (Multiplexion, Heidelberg). pSpCas9(BB-2A-GFP (PX458) and pSpCas9(BB)-2A-Puro (PX459) were a gift from Feng Zhang (Addgene plasmid #48138, 48139). A PX458 plasmid encoding a GFP-labeled Cas9 nuclease and the sgRNA sequence (from GECKO52 library #17446, GTGGTTAAACCATGTTAAGG, targeting first exon) was transfected into standard HeLa Kyoto cells with Lipofectamine 2000 following manufacturers instructions. Cells were cultured in DMEM media supplemented with 10% FBS and 1% penicillin-streptomycin at 37 °C and 5% CO_2. After three days, the transfected cells were FACS sorted by their GFP fluorescence into 96-well plates to obtain single clones and visually inspected53. These clones were then screened by Western blotting and in-del formation confirmed sequencing of genomic DNA (primer forward AGCGGCCGTCGCCACCG, reverse, TAAGCGCCTGCCGGGCTG). Note the region is extremely GC-rich (75%, +/- 250 nt from targeted indel region). Additionally, a mixed-clonal line was obtained by transfection of HeLa Kyoto with PX459 with the above sgRNA sequence. After 72 hours from transfection, cells were exchanged into media supplemented with 0.5 μg/mL puromycin (concentration determined in separated experiment) and selected for 3 days. All imaging experiments were confirmed on this secondary line.

Endocytosis rescue assays

Wild-type EEA1 and the extended and swapped variants (Extended Data Fig. 3) were cloned into customized mammalian expression plasmids under the CMV promoter resulting in untagged proteins. HeLa or HeLa EEA1-KO cells were seeded into 96-well plates and transfected (or mock transfected) after 48 hours. Following 48 hours after transfection, cells were exchanged into serum-free media containing 8.2 μg/mL LDL-Alexa 488 (prepared as previously described16) or 100 ng/mL EGF-Alexa 488 (E13345, Thermo Fisher) for 10 minutes at 37 °C , and washed in PBS then fixed in 4% paraformaldehyde.

Automated confocal immunofluorescence microscopy and analysis

Fixed cells were stained with antibodies against EEA1 (lab-made rabbit) and Rab5 (610724, prepared in mouse, BD Biosciences) as previously described24. DAPI was used to stain the nuclei. Not all early endosomes harbor EEA154 and other tethering factors could compensate for EEA124,55. All imaging was performed on a Yokogawa CV7000s automated spinning disc confocal using a 60x 1.2NA objective. 15 images were acquired per well and each condition was duplicated at least twice per plate, resulting in 30 or more images per condition.

Image analysis was performed in home-made software, MotionTracking, as previously described56,57. Images were first corrected for illumination, chromatic aberration and physical shift using multicolor beads. All cells, nuclei, and cell objects in corrected images were then segmented and their size, content, and complexity calculated. The intensity of EEA1 in wild-type HeLa cells was measured to determine a wild-type intensity distribution. In the rescue experiments, an intensity threshold for the transfections was set at ~2 times the mean of wild-type cells (Extended Data Fig. 8i). Experiments were repeated at different seeding densities with similar results. Given a cell density threshold between 10 and 100 per image, we obtained an average of more than 300 cells per condition after filtering for the transfection level of EEA1, and more than 15000 endosomes per experiment. Two-tailed t-test was used for significance calculations.

Cell electron microscopy

Cells in 3 cm diameter plastic dishes were processed for electron microscopy using a method58 to provide particularly heavy staining of cellular components. Briefly cells were fixed by addition of 2.5% glutaraldehyde in PBS for 1h at RT and then washed with PBS. The cells were then processed as described58 with sequential incubations in solutions containing potassium ferricyanide/osmium tetroxide, thiocarbohydrazide, osmium tetroxide, uranyl acetate and lead nitrate in aspartic acid before dehydration and flat embedding in resin. Sections were cut parallel to the substratum and analysed unstained in a Jeol1011 transmission electron microscope (Tokyo, Japan). Images for quantitation were collected from coded samples (double blind) to avoid bias.

Distance analysis was performed in ImageJ. To correct for thickness of slices (60 nm), the following equation was used:

$$P(R) = \frac{1}{Z}\int_0^H P_0\left(\sqrt{R^2 - h^2}\right)\frac{R}{\sqrt{R^2 - h^2}}dh,$$

where $P_0(r)$ is the apparent 2D distance distribution; R is the 3D distance, H is the thickness of the slice, and Z is the normalization constant. Uncorrected distance was measured at 119.8±78.2 nm (mean±SD), which resulted in 130.0±76.8 nm corrected.

Extended Data

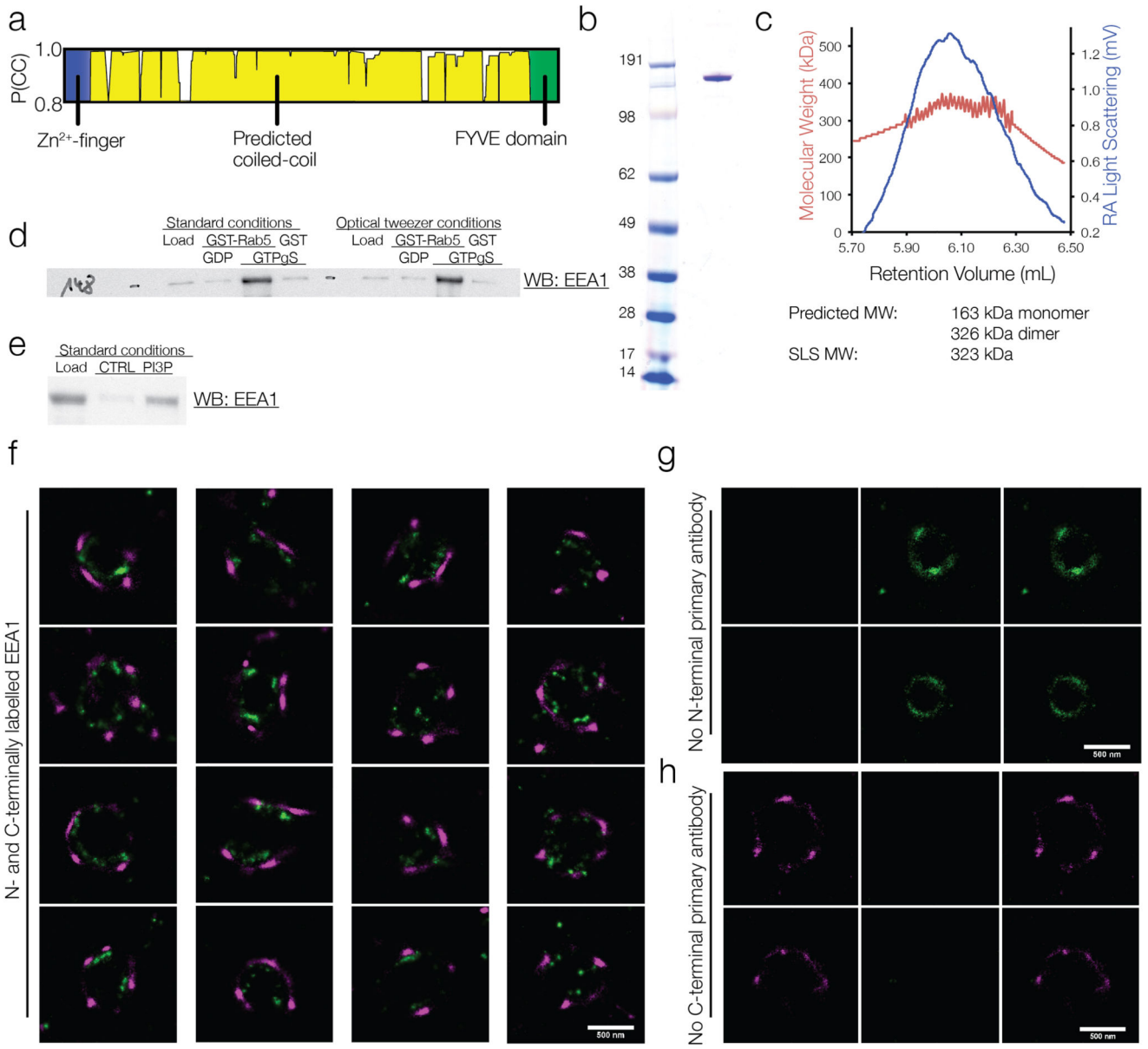

Extended Data Figure 1. EEA1 is a predicted extended coiled-coil dimer that binds Rab5 in a GTP dependent manner and extends outward from endosomes

Europe PMC Funders Author Manuscripts

Europe PMC Funders Author Manuscripts

a, Human EEA1 in COILS prediction reveals a clear coiled-structure flanked by the Rab5-binding Zn^{2+}-finger on the N-terminus and PI(3)P binding FYVE domain on the C-terminus.
b, Coomassie-stained gel of human EEA1 expressed as a GST fusion in SF+ insect cells and purified by GS affinity, cleaved on resin, and subsequently concentrated and separated from smaller contaminants by size-exclusion chromatography on a Superose 6 column.
c, Static light scattering in line with size-exclusion chromatography reveals a molecular weight of 323 kDa, compared to a theoretical molecular weight of 326 kDa for a dimeric protein.
d, Purified protein binds Rab5 in both standard and optical tweezers conditions (35% glycerol) in a GTP-dependent manner. GST or GST-Rab5 was purified and conjugated to GS resin, and subsequently nucleotide was exchanged to either GTPγS or GDP using EDTA-Mg^{2+} mediated exchange and subsequent wash. The GST resin was then incubated with EEA1 in either the standard or optical tweezers buffer, washed 3 times, and beads were then blotted for EEA1.
e, Recombinant EEA1 binds specifically to PI(3)P liposomes. When mixed with POPC:POPS 85:15 liposomes, no EEA1 is observed in the liposome pellet (CTRL). In contrast, EEA1 is pelleted with control POPC:POPS:PI(3)P 80:15:5 liposomes (PI3P).
f, The N-terminal Zn^{2+}-finger and C-terminal FYVE domain of EEA1 were differentially labeled with specific antibodies and STORM microscopy performed to define their localization in HeLa cells. Representative STORM images of EEA1 radial extension from endosome of n=22. Scale bar 500 nm.
g,h Primary antibody binding controls for N- and C-termini. Primary antibodies for the N- (g) and C- (h) termini were left out of the staining, resulting in no unspecific secondary staining for each. Representative of n=5. Scale bar 500 nm.

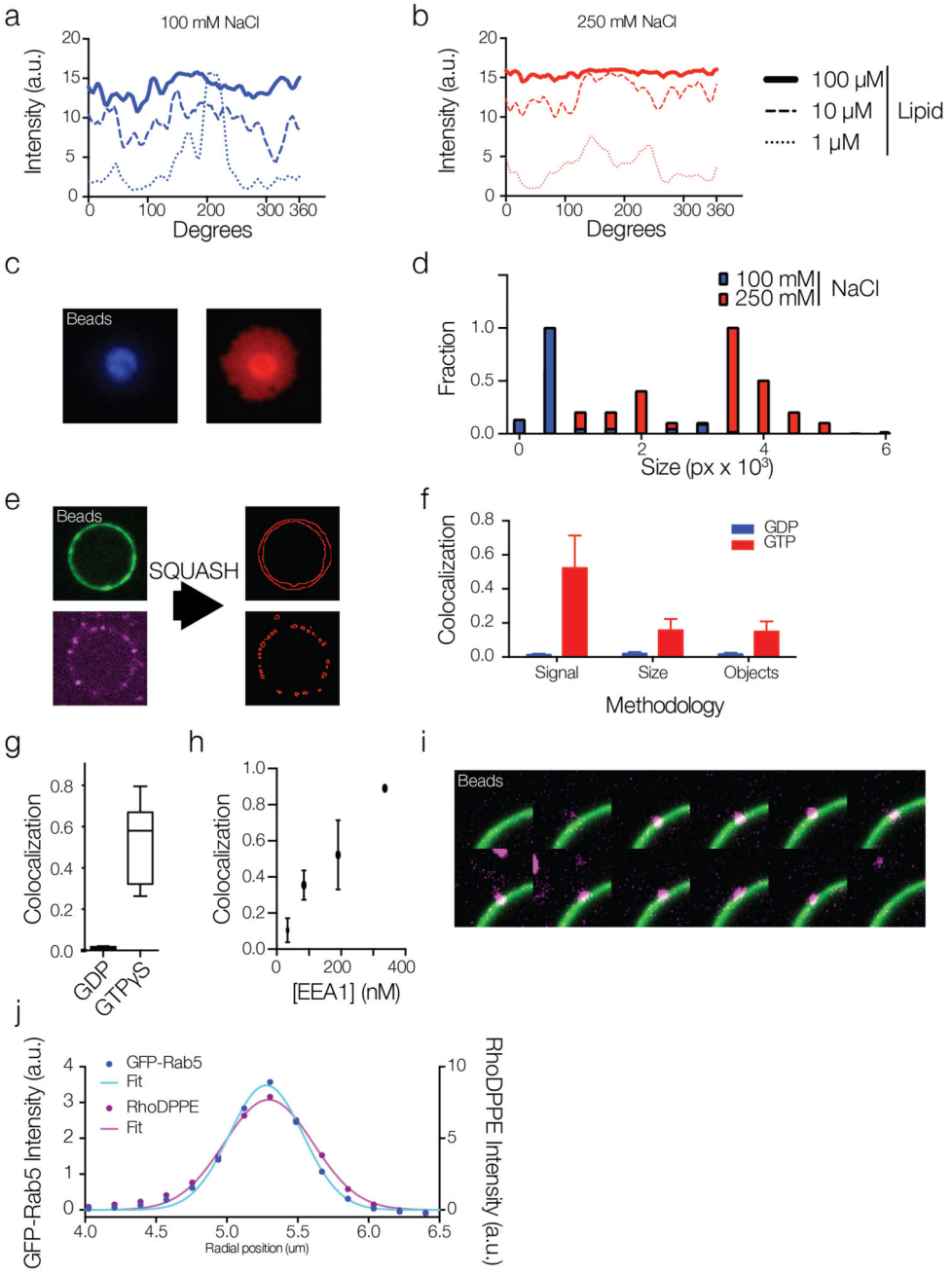

Extended Data Figure 2. Validation of bead-supported lipid bilayers for optical tweezers, and bead tethering experiment controls and methods

To optimize the conditions for forming supported lipid bilayers on the 2-10 μm beads, we systematically investigated the dependence of membrane formation on salt and liposome concentration.

a, Fluorescent profiles of supported lipid bilayer bead cross sections. At high liposome concentration (100 μM, solid line) during formation of the bilayer on the silica bead, the bead-supported membrane fluorescence intensity is circumferentially homogenous. At lower

Europe PMC Funders Author Manuscripts

lipid concentrations (10 and 1 μM, dashed and dotted lines), less than full coverage is achieved and the supported bilayer is inhomogeneous.

b, Consistent with previous reports, increasing salt concentrations result in more homogenous membrane coverage.

c, Representative examples of the “spilled-out” membrane of beads prepared at 100 mM (top, blue) and 250 mM (bottom, red) NaCl salt and 100 μm liposomes, of n=5.

d, Histogram of the size of membrane spilled from the beads onto the substrate when prepared at 100 and 250 mM NaCl (blue and red, respectively). This indicated that the lower salt samples (blue) were homogenously covered with membrane and that they had little excess present, and therefore the optimal conditions for formation of membrane on the silica beads used in tethering and in optical tweezer experiments.

e, Segmentation of beads and vesicles by the SQUASH method. Bead-supported bilayers and vesicles (green and magenta, respectively) were segmented as illustrated by red outlines to determine their colocalization. Representative of n=1 generated for schematic.

f, Methodology comparison for colocalization in GDP and GTPγS conditions. All methods give p<0.01 in two-tailed Student’s t-test. Colocalization by signal is better than size or object, as vesicles become undercounted at high concentrations. mean±s.d., n=5.

g, Colocalization of liposomes (PI(3)P, magenta) to the bead-supported membrane (GFP-Rab5, green) was strictly dependent on GTPγS. Box-whisker with min/max error, n=5.

h, The colocalization of liposomes to the supported membrane was dependent on EEA1 concentration. At higher concentrations of EEA1, colocalization approached 100%. These concentrations are within the range of the concentration of endogenous protein23. mean ±s.d., n=5.

i, Time-lapse micrographs of the bead-supported bilayer labeled with GFP-Rab5 (green), and a dynamically tethered vesicle (magenta). Vesicles were observed to tether and reversibly leave the membrane, as well as diffuse about its surface. Images displayed were acquired at 350 ms intervals as z-stacks. Representative of n=1 to acquire video. Scale bar 2 μm.

j, Example fits for radial line-profile data.

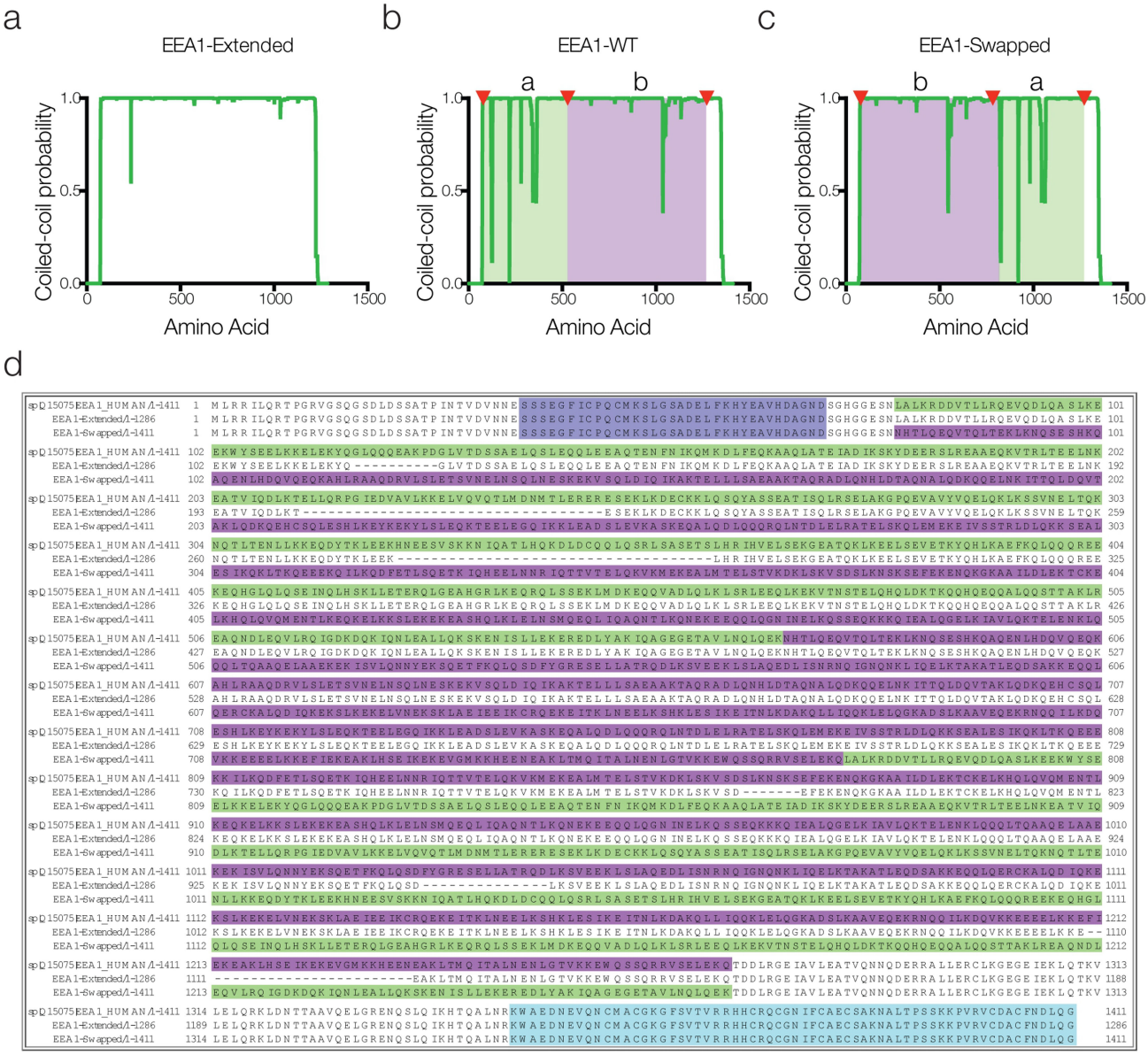

Extended Data Figure 3. Structure prediction and sequence description of EEA1 mutants

a, COILS prediction for extended EEA1 mutant, revealing removal of most of the discontinuities in the coiled-coil.

b, c The swapped EEA1 mutant has a rearranged coiled-coil. The coiled-coil was split as indicated by red triangles in the original EEA1-WT (b), and the two regions *a* (shaded green) and *b* (shaded magenta) were rearranged in a synthetic gene, producing the swapped EEA1 variant maintaining the features and sequence of the original coiled-coil, but in an alternative location (c).

d, Full sequence alignment for human EEA1 and the extended and swapped mutants used in the study. The crystal structure (PDB: 3MJH) for the Zn^{2+}-finger domain is marked in dark blue close to the N-terminus. Segment *a* of the coiled-coil region is marked in green, and

segment *b* in magenta. The crystal structure (PDB: 1JOC) of the C-terminal FYVE domain and portion of the coiled-coil is marked in cyan. Details of the mutant constructs are found in the Methods.

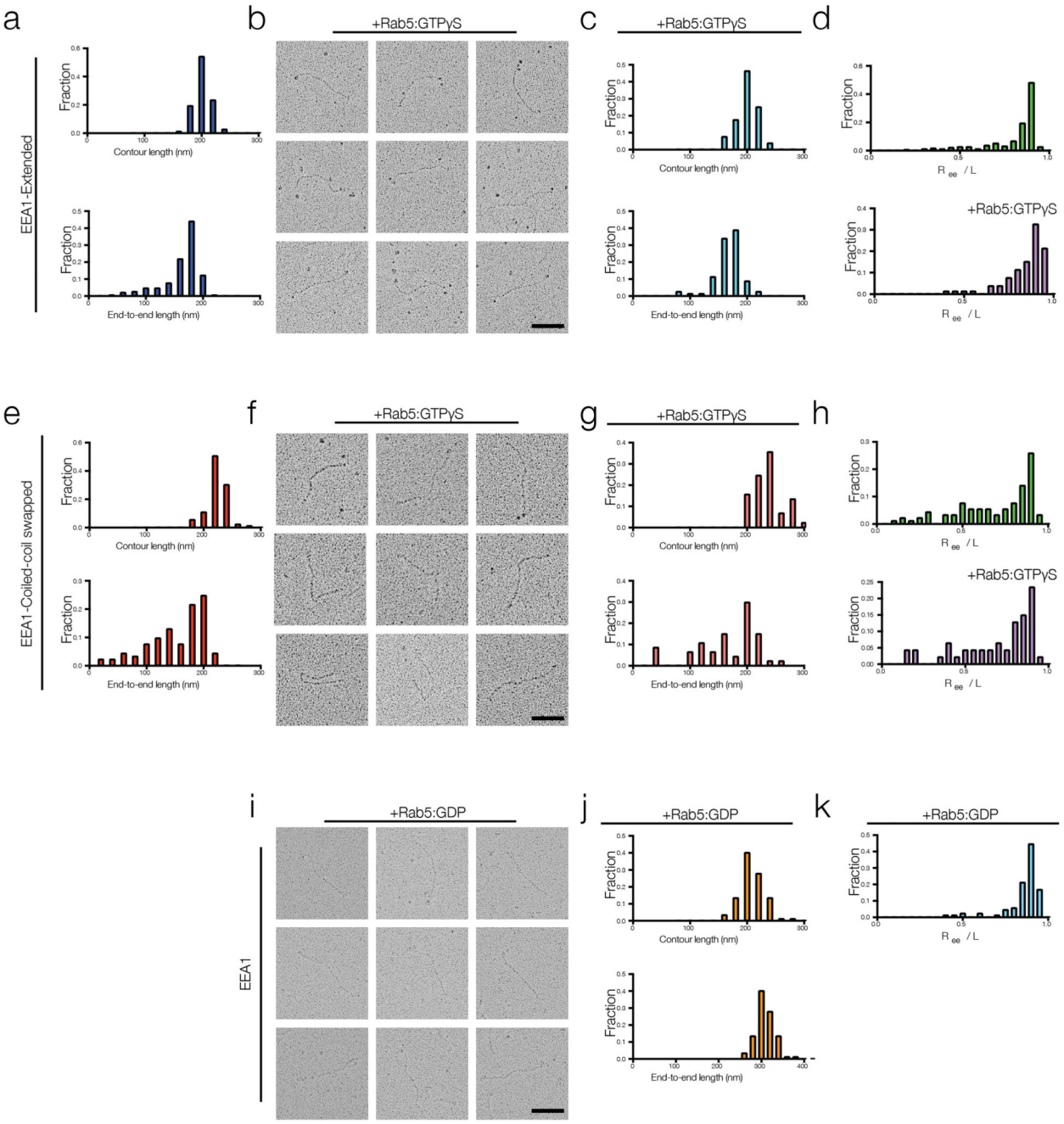

Extended Data Figure 4. Extended and Swapped EEA1 mutants exhibit limited changes in the presence of Rab5:GTPγS

a,e Rotary-shadowed EEA1-Extended particles and EEA1-Swapped mutants were skeletonized and analyzed in ImageJ for contour length (top), resulting in normally distributed contour length histograms. The end-to-end length histograms (bottom) are

similarly distributed. These data were collected on N-terminally MBP-tagged samples. Compare with wild-type in Fig. 2b,d. n=212 for the extended and n=93 for the swapped variants.

b-d,f-g,The mutant EEA1s revealed limited changes to their curvature in the presence of Rab5:GTPγS (b,f; compare Fig. 2i,j), and therefore minor changes to their contour and end-to-end length histograms (c,g), and radial distribution plots (d,h). n=80 for the extended and n=47 for the swapped variants.

i-j, Rotary-shadowing electron microscopy of EEA1 in the presence of Rab5:GDP (n=90), N-terminally MBP-tagged, revealed no change in appearance compared to the absence of Rab5 entirely (Fig. 2a), and no effect of N-terminal tagging relative to wild-type EEA1.

k, Radial distribution function of EEA1 in the presence of Rab5:GDP (compare d, h; Fig. 2g). n=90.

Europe PMC Funders Author Manuscripts

Europe PMC Funders Author Manuscripts

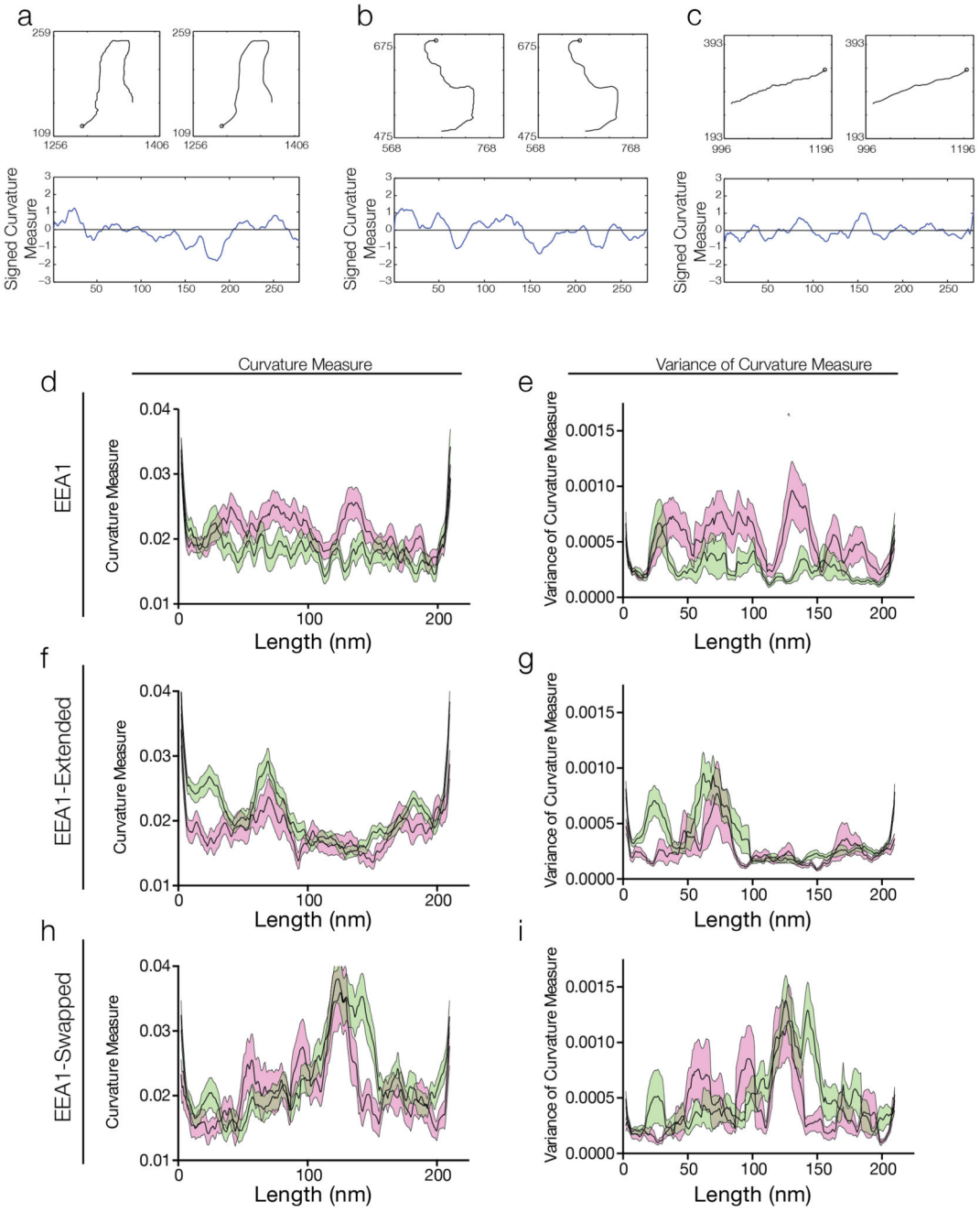

Extended Data Figure 5. Representative segmentation, smoothing, and signed curvature measures for EEA1, and averages for EEA1 and mutants.

EEA1 and EEA1 mutants were skeletonized and smoothed using a moving average filter with a window of 8.2 nm, segmented to 300 equally spaced segments, and aligned N-terminal to C- by recognition of an N-terminal MBP-tag. Their curvature was calculated at 15 nm distances along the length of the proteins and plotted.

a-c Representative examples of rotary shadowing derived EEA1 curves. The original data appears in the first panel, with the second panel revealing the data after smoothing for comparison (Methods). The curvature measure, determined by how the tangents to the

Europe PMC Funders Author Manuscripts

contour change at a distance of 15 nm along the contour is plotted below. Note that the choice of sign for the curvature measure is arbitrary for each molecule.

d,e Curvature measure and variance of this measure for EEA1 in the presence of Rab5:GDP (green) and EEA1 in the presence of Rab5:GTPγS (magenta). Alignment of EEA1 curvature from the electron microscopy data reveals an increase in curvature over the length of the molecule upon Rab5 binding, whereas the extended and swapped EEA1 variants show no change. All curvature values were taken to be positive given that the N-terminal MBP could be recognized but the handedness of the molecule adsorbed to the grid could not be inferred. Bootstrapping with resampling at full population size was performed for 1000 iterations to determine errors. n=90, n=145, respectively.

f,g Extended EEA1 variant in the absence (green) and in the presence of Rab5:GTPγS (magenta). n=212, n=80, respectively.

h,i Swapped EEA1 variant in the absence (green) and in the presence of Rab5:GTPγS (magenta). n=93, n=47, respectively.

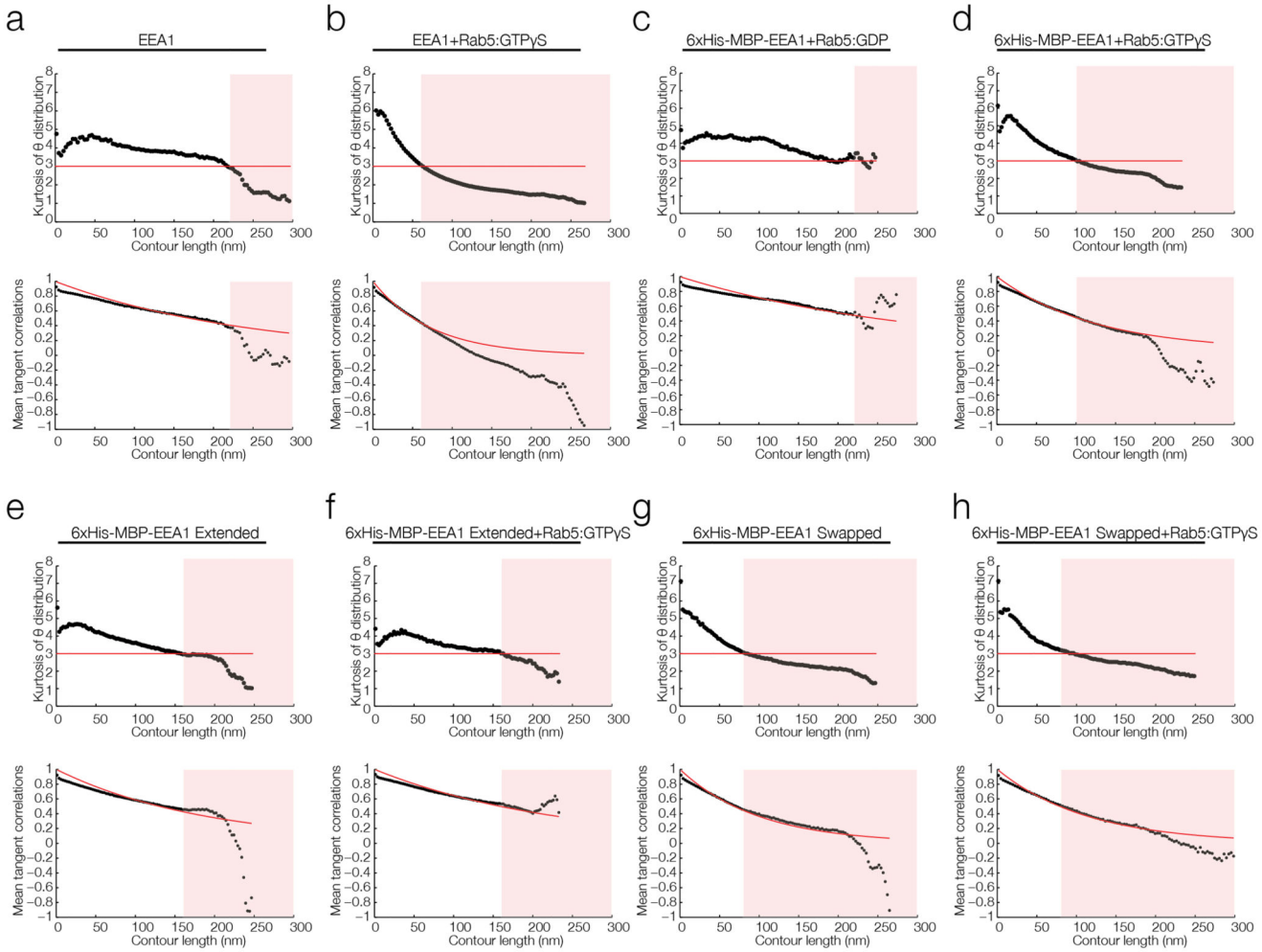

Extended Data Figure 6. Detailed persistence length and equilibration analysis for EEA1 and variants

To validate the methodology used for analysis of the persistence lengths, and to assure internal consistency in analysis methods, we systematically applied the analysis to EEA1 (and mutants, see Extended Data Table 1). The skeletonized curves were segmented to 300 equally spaced segments, where θ describes the angle between segments. The tangent-tangent correlations were then determined for the entire ensembles.

a-h To determine the molecular equilibration of EEA1 and variants from 3D to 2D, the kurtosis of the theta distribution (top) was calculated. Full equilibration to 2D gives a value of 3.0, and for 3D is the expected value is 1.8 as the angle distributions become Gaussian. As expected, the measured kurtosis is approximately 3.0 until lengths above the persistence length of the molecule, where the equilibration begins to fail. The value at which the kurtosis began to diverge from 2D was taken as the limit for subsequent measurements, as beyond this limit (red shaded region) 3D fluctuations are not retained and as such the consequences of surface adsorption are uncertain. Next, the tangent-tangent correlation was calculated across the ensemble and fit up to the divergence of the kurtosis (red shaded region).

Europe PMC Funders Author Manuscripts

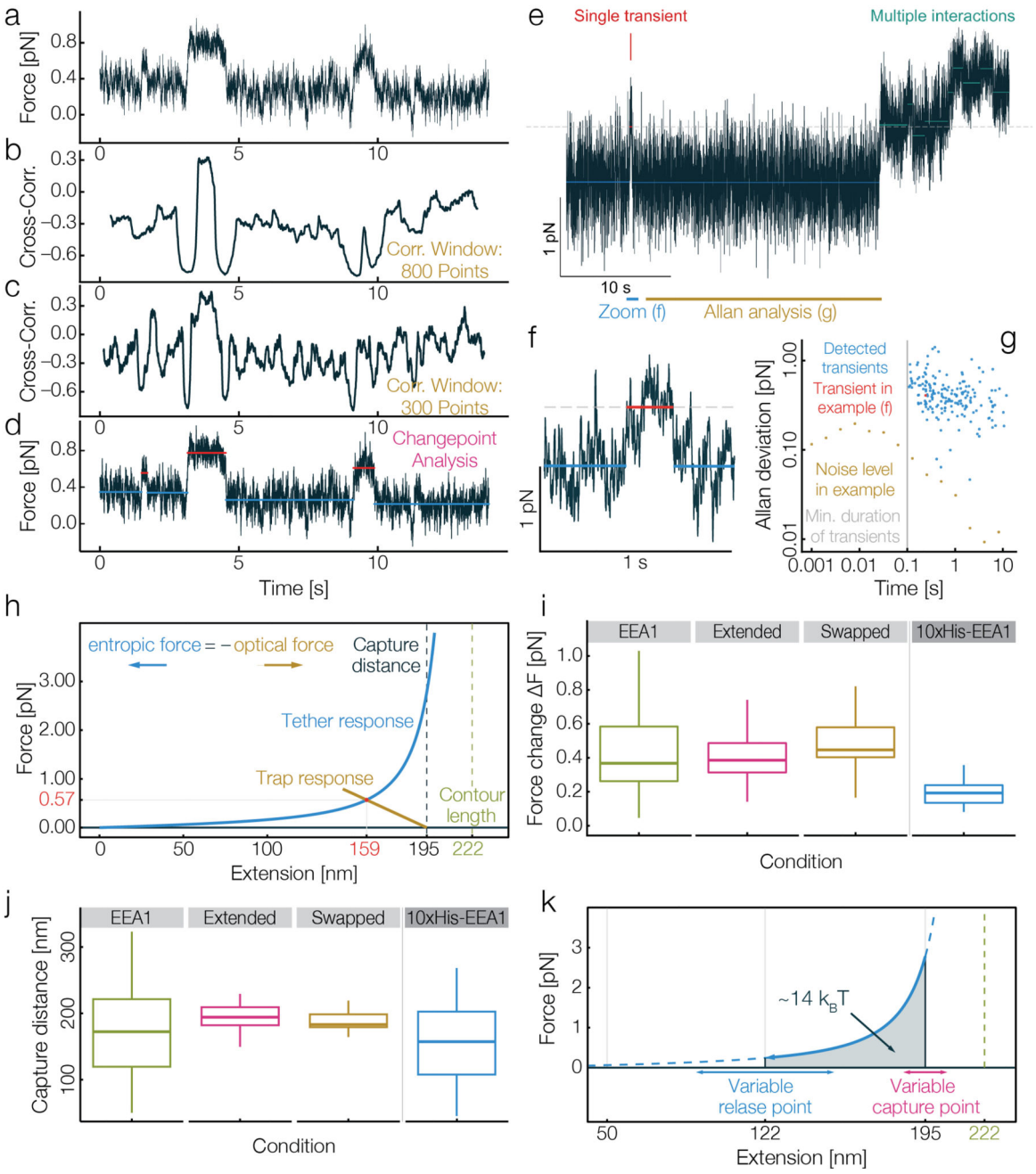

Extended Data Figure 7. Supplemental data related to optical tweezer experiments

a, Changepoint analysis was used to identify changes in mean and variance of combined force signal. An example plot of averaged force (linear combination of signals from both traps) with respect to time. Data has been collected at 1 kHz. Two long transient interactions can be clearly identified.

b,c Cross-correlation of the force signals from each trap are not sufficient to reveal stepwise interactions as they are time-averaged. By applying cross-correlation over a correlation window of 0.8 s (b) or 0.3 s (c), long transient interactions (i.e. at ~4 s) could be identified.

However, an unbiased identification of short transients (i.e. at ~9 s) by this method was not possible. All identified long transient interactions showed characteristic changes in the cross-correlation: anti-correlation as beads are pulled together, and correlation after tethering was established.

d, Changepoint analysis was used to detect both changes in mean and variance of the combined force signal, and thereby identify transient interactions (red line). This procedure has the additional advantage of defining clear boundaries to stepwise processes.

e, The possibility of multiple tethers taking part in the reaction was observed. Averaged force trace for wild-type EEA1,occasionally showed signals consistent with multiple interactions (cyan), in addition to single transient interactions (red).

f, Zoom into time-series around the transient interaction identified in previous panel. To a first approximation, the dynamic interactions were fit as piecewise constant steps (red). Note also two very short (<10 ms) spikes of similar magnitude (to the left and right of identified interaction) occurred but are not used in further analysis. Only transients with a duration longer than 100 ms were analyzed.

g, To illustrate the sensitivity of the optical tweezer experiments, a noise analysis was performed on the segment outlined in the top panel (yellow, labeled Allan analysis). The Allan deviation (square root of Allan variance, in pN) gives a threshold for detecting a signal change over different averaging windows. All detected transients (blue) are at minimum an order of magnitude above this threshold. To provide perspective, the transient in the above example is indicated as a red dot.

h, The entropic collapse force is balanced in the tweezer experiments below its peak value. The balance between the average restoring force in the optical traps (brown) and the entropic collapse force of EEA1 (blue) in the bound state gives the measured equilibrium force and extension (red dot). The schematic assumes the measured capture distance of 195 nm, a persistence length in the Rab5:GTP-bound state of λ_b = 26 nm, and a contour length of 222 nm. The overall trap response of the dual-trap system is treated as two springs in series with the mean trap stiffness in trap 1 ($\kappa 1$ = 0.035±0.007 pNnm^{-1}) and the mean trap stiffness in trap 2 ($\kappa 2$ = 0.029±0.007 pNnm^{-1}), leading to an overall trap stiffness of κT = 0.0159 pNnm^{-1} (brown line). Given these parameters, the predicted equilibrium force in the optical trap for Rab5-bound EEA1 is ~0.6 pN and the predicted equilibrium extension ~160 nm.

i, Force changes upon capture for Rab5:GTP-bound EEA1 and the extended and swapped variants. Force was measured from change-point analysis for transient interactions between EEA1 beads and Rab5:GTP beads. To test binding *per se*, the force change for 10xHis-EEA1 beads tethered to Ni-NTA beads was similarly determined from established connections. For 10xHis-EEA1, no transient interactions could be observed. Median change in force and 95% Confidence Interval from bootstrapping with resampling (lower and upper bounds at [2.5%, 97.5%]) were determined. EEA1, 0.37 [0.31, 0.46] pN. Extended, 0.39 [0.35, 0.42] pN. Swapped, 0.45 [0.41, 0.56] pN. 10xHis, 0.19 [0.14, 0.22] pN.

j Capture distances defined at the proximal distance upon which transient interactions were observed for Rab5 bound EEA1 and the extended and swapped variants. Median capture distance and 95% Confidence Interval from bootstrapping with resampling (lower and upper bounds at [2.5%, 97.5%]) were determined. EEA1, 168 [141, 182] nm. Extended, 195 [189, 199] nm. Swapped, 183 [179, 189] nm. 10xHis, 157 [120, 196] nm. n = 60, 93, 27, 24 per condition respectively.

k, Mechanical work is performed as the tether collapses. The mechanical work performed during the relaxation to the new equilibrium extension is the integral under the force-extension curve. The exact value of the extracted work depends both on the capture distance (the extension at the moment of persistence length change), and on the release distance (the extension at the moment when Rab5 unbinds). The uncertainties in these extensions are different for the two positions, reflecting the different longitudinal fluctuations of the rigid or the flexible tether ($\lambda_{flexible}$ = 26 nm [blue arrows], λ_{rigid} = 300 nm [magenta arrows]). For a relaxation between the capture distance, $d_{capture} \approx$ 195 nm, and the release extension, $d_{release} \approx$ 122 nm, the extracted mechanical work is $W \approx 14\ k_B T$.

Europe PMC Funders Author Manuscripts

Europe PMC Funders Author Manuscripts

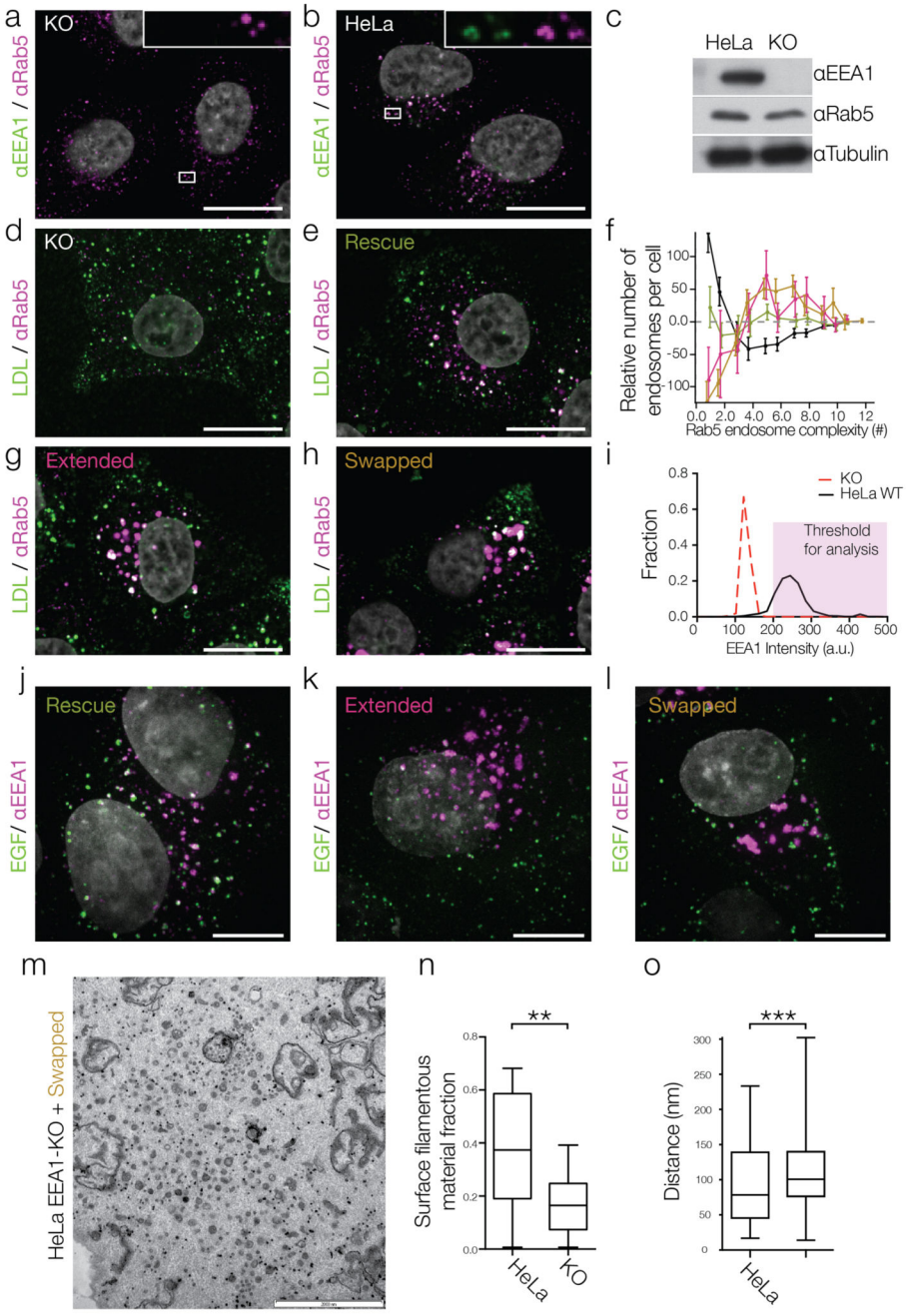

Extended Data Figure 8. EEA1 mutants incapable of undergoing entropic collapse result in defects in endosomal trafficking.

a, b Automated confocal immunofluorescence images (*n*=30 each) of HeLa EEA1-KO and standard HeLa cells. EEA1 (green) and Rab5 (magenta). Scale bar 10 μm.

c, Western blot of HeLa and HeLa EEA1-KO clonal cell line for EEA1 and Rab5.

d,e,g,h Automated confocal images (*n*=30 each) of HeLa EEA1-KO cells expressing no EEA1 (KO, d), rescued with wild-type EEA1 (Rescue, e) or Extended and Swapped mutants (g,h). Cells were pulsed with fluorescently labeled cargo (LDL) (green) for 10 minutes,

Europe PMC Funders Author Manuscripts

fixed, and immunostained for Rab5 (magenta) and EEA1 (for EEA1, see Figure 4). Magnified insets of endosomes are depicted at arrows. Scale bar 10 μm.

f, Relative complexity of Rab5 endosomes per cell. Each Rab5 endosome is segmented, and the segmented object requires a defined number of 2D Gaussian functions, hereby referred to as complexity. Relative to wild-type, HeLa EEA1-KOs (black line) had a significantly reduced number of endosomes of high complexity (>3.0), but more endosomes defined simply by 1 or 2 Gaussian functions. Rescue experiments (red) revealed no significant difference in complexity. In contrast, both extended and swapped mutants (blue and green respectively) had significantly fewer simple endosomes of low complexity, and significantly more of higher complexity. mean±s.d., n=30.

i, Histogram of fluorescence intensity of EEA1 per cell. KO cell lines had a sharp peak of intensity at background levels, whereas wild-type HeLa cells had a normal distribution. Grey box represents threshold levels of EEA1 intensity per cell taken for analysis.

j-l EGF uptake experiments. Confocal images of HeLa EEA1-KOs expressing wild-type EEA1 (Rescue, j) or Extended and Swapped mutants (g,h). Cells were pulsed with fluorescently labeled EGF (green) for 10 minutes, fixed, and immunostained for EEA1 (magenta). Images shown are maximum intensity projections. Scale bar 5 μm.

m, HeLa EEA1-KO cells in which the Swapped EEA1 mutant was reintroduced showed clusters of vesicles and more rarely the classical endosomal morphology. The clusters were clearly delineated by a zone of cytoplasm with a distinct density. Representative of n=19. Scale bars, 2 μm.

n, Further quantifications, and the swapped mutant ultrastructural phenotype. Fraction of endosomal surface containing filamentous material for HeLa and HeLa EEA1-KOs. Box-whisker plot with minimum/maximum values, n=22, 24 endosomes. **, $p<0.01$, two-tailed Students t-test.

o, Distance measured between endosome and tethered vesicles (HeLa) or between vesicles within large clusters (Extended) (surface-to-surface, n=158 and 623 for HeLa and Extended respectively. ***, $p<10^{-4}$, two-tailed Students t-test.).

Europe PMC Funders Author Manuscripts

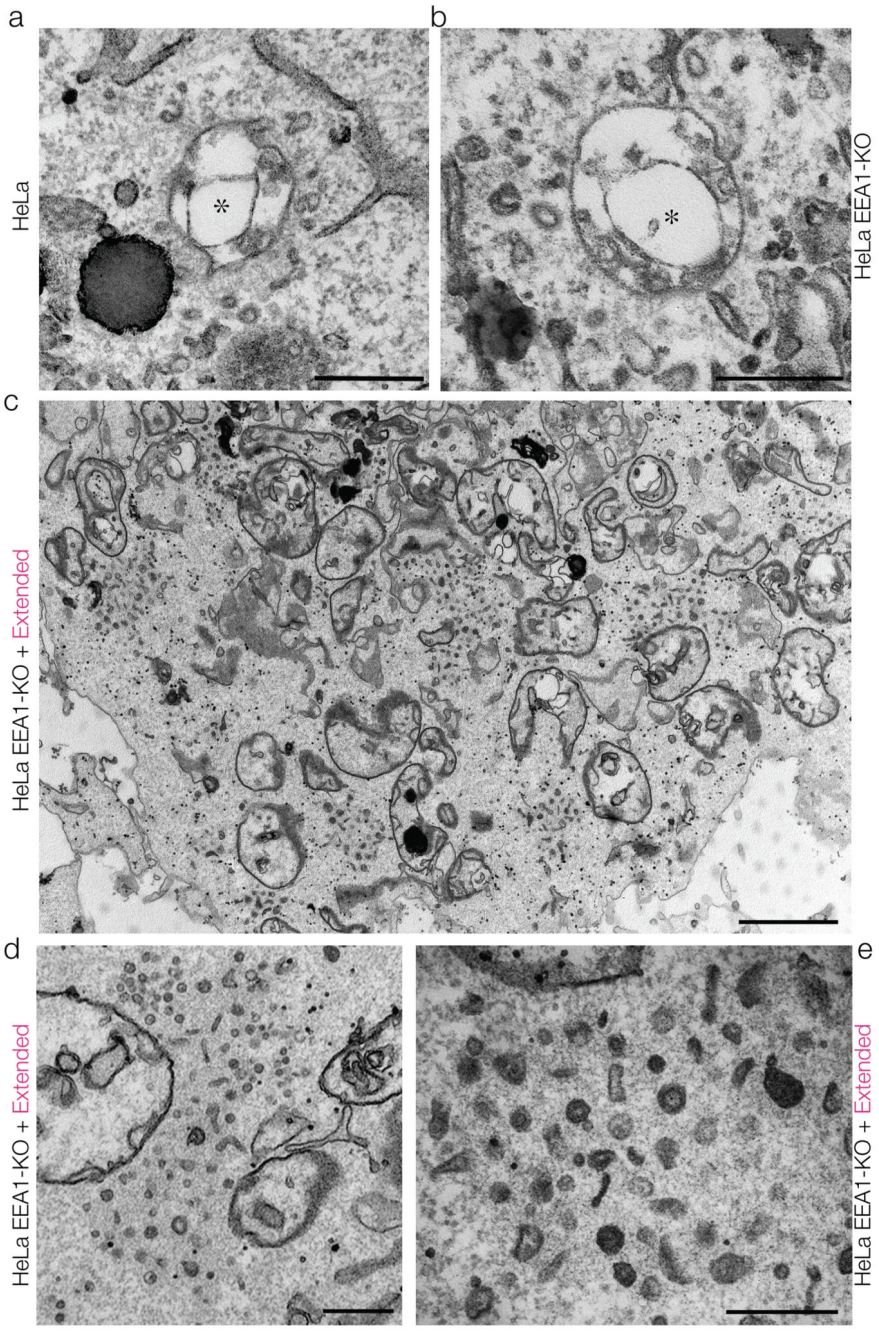

Extended Data Figure 9.
Unlabeled version of Figure 5

Europe PMC Funders Author Manuscripts

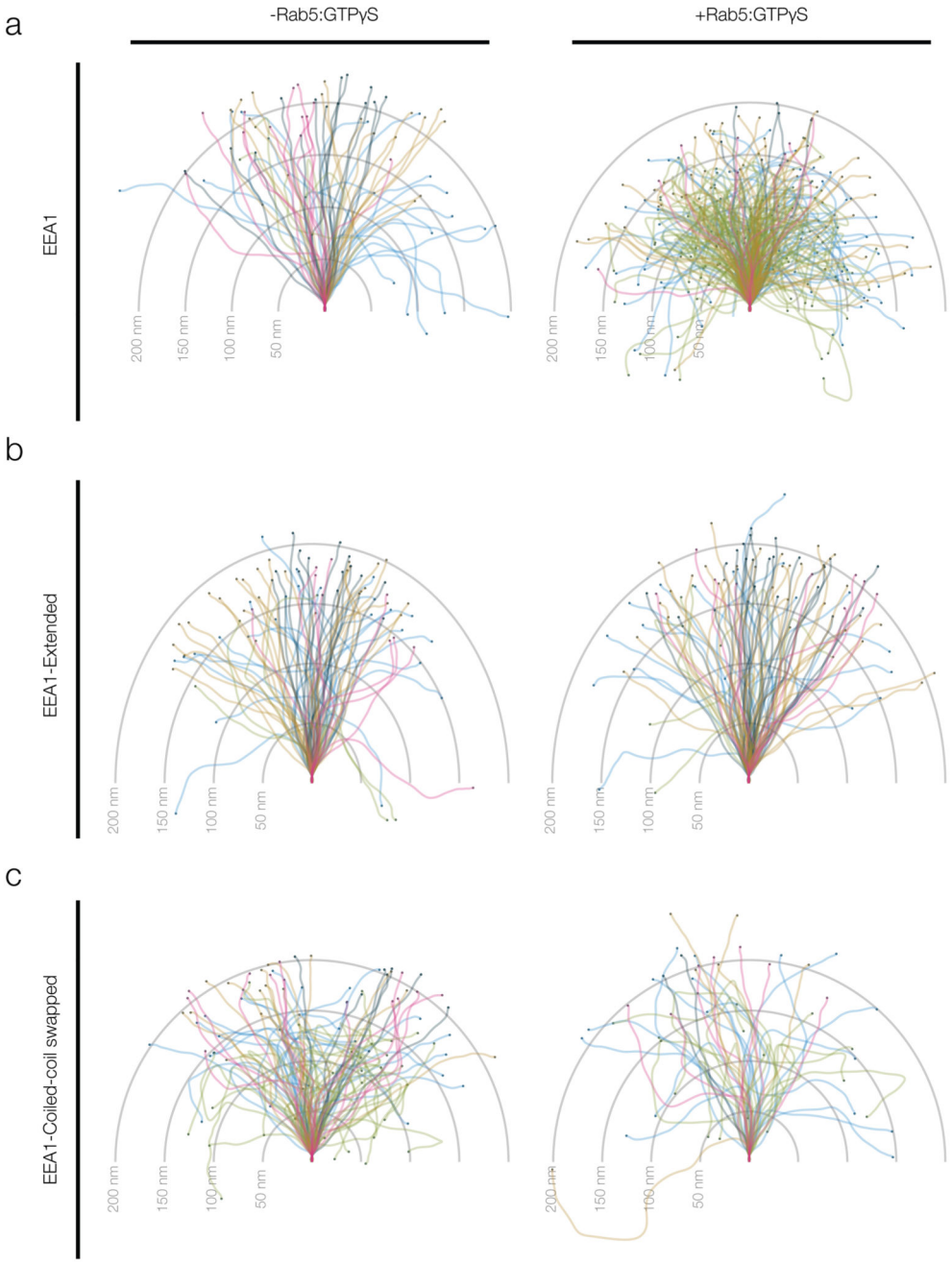

Extended Data Figure 10.

Bouquet plots of EEA1 and variants. EEA1 in the absence of Rab5 is predominantly extended. The initial five segments of the curves from rotary shadowing EM were aligned and the curves plotted with the end position highlighted (dots). Grey concentric hemispheres demarcate 50, 100, 150 and 200 nm extensions from the origin. The end positions therefore resulted in a cloud of empirical positions for the EEA1 N-terminus of EEA1 (left), and reveal the overall change in conformational space that can be occupied by EEA1 when bound to Rab5:GTPγS (right).

b, Bouquet plots for the extended EEA1 variant.

c, Bouquet plots for the swapped EEA1 variant.

Supplementary Material

Refer to Web version on PubMed Central for supplementary material.

Acknowledgements

We thank Ramona Schäfer for invaluable project support. We acknowledge fruitful discussions with José Morin, Ünal Coskun, Alf Honigmann, Sebastian Sturm and Thomas Leonard, and Frank Jülicher, Erik Schäfer, and Kai Simons for a critical reading of the manuscript. We thank Marlene Brandstetter and the Electron Microscopy facility of the Vienna Biocenter. We thank the Light Microscopy, Protein Expression, Chromatography, and High-throughput Technology Development Studio of the Max Planck Institute of Molecular Cell Biology and Genetics. During part of the work, M.J. was supported by a PhD scholarship of the Böhringer Ingelheim Fonds. R.P. was supported by the National Health and Medical Research Council (NHMRC) of Australia (program grant, APP1037320 and Senior Principal Research Fellowship, 569452), and the Australian Research Council Centre of Excellence (CE140100036). We acknowledge the Australian Microscopy & Microanalysis Research Facility at the Center for Microscopy and Microanalysis at The University of Queensland. S.W.G. was supported by the DFG (SPP 1782, GSC 97, GR 3271/2, GR 3271/3, GR 3271/4), the European Research Council (grant No 281903) and the Human Frontier Science Program (RGP0023/2014). This research was supported by the Max Planck Society and funds of the Deutsche Forschungsgemeinschaft (Transregio 83).

References

1. Brocker C, Engelbrecht-Vandre S, Ungermann C. Multisubunit tethering complexes and their role in membrane fusion. Current biology : CB. 2010; 20:R943–952. DOI: 10.1016/j.cub.2010.09.015 [PubMed: 21056839]
2. Brown FC, Pfeffer SR. An update on transport vesicle tethering. Molecular membrane biology. 2010; 27:457–461. DOI: 10.3109/09687688.2010.501765 [PubMed: 21067454]
3. Zerial M, McBride H. Rab proteins as membrane organizers. Nature reviews Molecular cell biology. 2001; 2:107–117. DOI: 10.1038/35052055 [PubMed: 11252952]
4. Munro S. Organelle identity and the organization of membrane traffic. Nature cell biology. 2004; 6:469–472. DOI: 10.1038/ncb0604-469 [PubMed: 15170453]
5. Mayer A, Wickner W. Docking of yeast vacuoles is catalyzed by the Ras-like GTPase Ypt7p after symmetric priming by Sec18p (NSF). The Journal of cell biology. 1997; 136:307–317. [PubMed: 9015302]
6. Christoforidis S, McBride HM, Burgoyne RD, Zerial M. The Rab5 effector EEA1 is a core component of endosome docking. Nature. 1999; 397:621–625. DOI: 10.1038/17618 [PubMed: 10050856]
7. Rubino M, Miaczynska M, Lippe R, Zerial M. Selective membrane recruitment of EEA1 suggests a role in directional transport of clathrin-coated vesicles to early endosomes. The Journal of biological chemistry. 2000; 275:3745–3748. [PubMed: 10660521]
8. Gao Y, et al. Single reconstituted neuronal SNARE complexes zipper in three distinct stages. Science. 2012; 337:1340–1343. DOI: 10.1126/science.1224492 [PubMed: 22903523]
9. Kiessling V, Tamm LK. Measuring distances in supported bilayers by fluorescence interference-contrast microscopy: polymer supports and SNARE proteins. Biophysical journal. 2003; 84:408–418. DOI: 10.1016/S0006-3495(03)74861-9 [PubMed: 12524294]
10. Dumas JJ, et al. Multivalent endosome targeting by homodimeric EEA1. Molecular cell. 2001; 8:947–958. [PubMed: 11741531]
11. Wilson JM, et al. EEA1, a tethering protein of the early sorting endosome, shows a polarized distribution in hippocampal neurons, epithelial cells, and fibroblasts. Molecular biology of the cell. 2000; 11:2657–2671. [PubMed: 10930461]
12. Simonsen A, et al. EEA1 links PI(3)K function to Rab5 regulation of endosome fusion. Nature. 1998; 394:494–498. DOI: 10.1038/28879 [PubMed: 9697774]

Europe PMC Funders Author Manuscripts

13. Mishra A, Eathiraj S, Corvera S, Lambright DG. Structural basis for Rab GTPase recognition and endosome tethering by the C2H2 zinc finger of Early Endosomal Autoantigen 1 (EEA1). Proceedings of the National Academy of Sciences of the United States of America. 2010; 107:10866–10871. DOI: 10.1073/pnas.1000843107 [PubMed: 20534488]
14. Lupas A, Van Dyke M, Stock J. Predicting coiled coils from protein sequences. Science. 1991; 252:1162–1164. DOI: 10.1126/science.252.5009.1162 [PubMed: 2031185]
15. McDonnell AV, Jiang T, Keating AE, Berger B. Paircoil2: improved prediction of coiled coils from sequence. Bioinformatics. 2006; 22:356–358. DOI: 10.1093/bioinformatics/bti797 [PubMed: 16317077]
16. Rink J, Ghigo E, Kalaidzidis Y, Zerial M. Rab conversion as a mechanism of progression from early to late endosomes. Cell. 2005; 122:735–749. DOI: 10.1016/j.cell.2005.06.043 [PubMed: 16143105]
17. Landau, LD.; Lifshitz, EM. Statistical Physics, Part 1. 3rd Edition edn. Vol. 5. Butterworth-Heinemann; 1980. Chapter 12
18. Wilhelm J, Frey E. Radial distribution function of semiflexible polymers. Physical review letters. 1996; 77:2581–2584. DOI: 10.1103/Physrevlett.77.2581 [PubMed: 10061990]
19. Otto O, Sturm S, Laohakunakorn N, Keyser UF, Kroy K. Rapid internal contraction boosts DNA friction. Nature communications. 2013; 4:1780.doi: 10.1038/ncomms2790
20. Rybin V, et al. GTPase activity of Rab5 acts as a timer for endocytic membrane fusion. Nature. 1996; 383:266–269. DOI: 10.1038/383266a0 [PubMed: 8805704]
21. Milner ST. Polymer brushes. Science. 1991; 251:905–914. DOI: 10.1126/science.251.4996.905 [PubMed: 17847384]
22. Degtyar VE, Allersma MW, Axelrod D, Holz RW. Increased motion and travel, rather than stable docking, characterize the last moments before secretory granule fusion. Proceedings of the National Academy of Sciences of the United States of America. 2007; 104:15929–15934. DOI: 10.1073/pnas.0705406104 [PubMed: 17893335]
23. Ohya T, et al. Reconstitution of Rab- and SNARE-dependent membrane fusion by synthetic endosomes. Nature. 2009; 459:1091–1097. DOI: 10.1038/nature08107 [PubMed: 19458617]
24. Perini ED, Schaefer R, Stoter M, Kalaidzidis Y, Zerial M. Mammalian CORVET is required for fusion and conversion of distinct early endosome subpopulations. Traffic. 2014; 15:1366–1389. DOI: 10.1111/tra.12232 [PubMed: 25266290]
25. Moreno-Herrero F, et al. Mesoscale conformational changes in the DNA-repair complex Rad50/Mre11/Nbs1 upon binding DNA. Nature. 2005; 437:440–443. DOI: 10.1038/nature03927 [PubMed: 16163361]
26. Taylor KC, et al. Skip residues modulate the structural properties of the myosin rod and guide thick filament assembly. Proceedings of the National Academy of Sciences of the United States of America. 2015; 112:E3806–3815. DOI: 10.1073/pnas.1505813112 [PubMed: 26150528]
27. Cheung PY, Limouse C, Mabuchi H, Pfeffer SR. Protein flexibility is required for vesicle tethering at the Golgi. eLife. 2015; 4doi: 10.7554/eLife.12790
28. Schmidt H, Zalyte R, Urnavicius L, Carter AP. Structure of human cytoplasmic dynein-2 primed for its power stroke. Nature. 2015; 518:435–438. DOI: 10.1038/nature14023 [PubMed: 25470043]
29. Kon T, et al. Helix sliding in the stalk coiled coil of dynein couples ATPase and microtubule binding. Nature structural & molecular biology. 2009; 16:325–333. DOI: 10.1038/nsmb.1555
30. Sheffield P, Garrard S, Derewenda Z. Overcoming expression and purification problems of RhoGDI using a family of “parallel” expression vectors. Protein expression and purification. 1999; 15:34–39. DOI: 10.1006/prep.1998.1003 [PubMed: 10024467]
31. Delprato A, Merithew E, Lambright DG. Structure, exchange determinants, and family-wide rab specificity of the tandem helical bundle and Vps9 domains of Rabex-5. Cell. 2004; 118:607–617. DOI: 10.1016/j.cell.2004.08.009 [PubMed: 15339665]
32. Horiuchi H, et al. A novel Rab5 GDP/GTP exchange factor complexed to Rabaptin-5 links nucleotide exchange to effector recruitment and function. Cell. 1997; 90:1149–1159. [PubMed: 9323142]
33. Boura E, Hurley JH. Structural basis for membrane targeting by the MVB12-associated beta-prism domain of the human ESCRT-I MVB12 subunit. Proceedings of the National Academy of Sciences

Europe PMC Funders Author Manuscripts

of the United States of America. 2012; 109:1901–1906. DOI: 10.1073/pnas.1117597109 [PubMed: 22232651]

34. Murray DH, Tamm LK, Kiessling V. Supported double membranes. Journal of structural biology. 2009; 168:183–189. DOI: 10.1016/j.jsb.2009.02.008 [PubMed: 19236921]
35. Neumann S, Pucadyil TJ, Schmid SL. Analyzing membrane remodeling and fission using supported bilayers with excess membrane reservoir. Nature protocols. 2013; 8:213–222. DOI: 10.1038/nprot.2012.152 [PubMed: 23288321]
36. Pucadyil TJ, Schmid SL. Real-time visualization of dynamin-catalyzed membrane fission and vesicle release. Cell. 2008; 135:1263–1275. DOI: 10.1016/j.cell.2008.11.020 [PubMed: 19084268]
37. Rizk A, et al. Segmentation and quantification of subcellular structures in fluorescence microscopy images using Squassh. Nature protocols. 2014; 9:586–596. DOI: 10.1038/nprot.2014.037 [PubMed: 24525752]
38. Lo SY, et al. Intrinsic tethering activity of endosomal Rab proteins. Nature structural & molecular biology. 2012; 19:40–47. DOI: 10.1038/nsmb.2162
39. Tyler JM, Branton D. Rotary shadowing of extended molecules dried from glycerol. Journal of ultrastructure research. 1980; 71:95–102. [PubMed: 6155474]
40. Gittes F, Mickey B, Nettleton J, Howard J. Flexural rigidity of microtubules and actin filaments measured from thermal fluctuations in shape. The Journal of cell biology. 1993; 120:923–934. [PubMed: 8432732]
41. Eeftens JM, et al. Condensin Smc2-Smc4 Dimers Are Flexible and Dynamic. Cell reports. 2016; 14:1813–1818. DOI: 10.1016/j.celrep.2016.01.063 [PubMed: 26904946]
42. Lamour G, Kirkegaard JB, Li H, Knowles TP, Gsponer J. Easyworm: an open-source software tool to determine the mechanical properties of worm-like chains. Source code for biology and medicine. 2014; 9:16.doi: 10.1186/1751-0473-9-16 [PubMed: 25093038]
43. Rivetti C, Guthold M, Bustamante C. Scanning force microscopy of DNA deposited onto mica: equilibration versus kinetic trapping studied by statistical polymer chain analysis. Journal of molecular biology. 1996; 264:919–932. DOI: 10.1006/jmbi.1996.0687 [PubMed: 9000621]
44. Valle F, Favre M, De Los Rios P, Rosa A, Dietler G. Scaling exponents and probability distributions of DNA end-to-end distance. Physical review letters. 2005; 95:158105.doi: 10.1103/PhysRevLett.95.158105 [PubMed: 16241768]
45. Lisica A, et al. Mechanisms of backtrack recovery by RNA polymerases I and II. Proceedings of the National Academy of Sciences of the United States of America. 2016; 103:2946–2951. DOI: 10.1073/pnas.1517011113
46. Jahnel M, Behrndt M, Jannasch A, Schaffer E, Grill SW. Measuring the complete force field of an optical trap. Optics letters. 2011; 36:1260–1262. DOI: 10.1364/OL.36.001260 [PubMed: 21479051]
47. Czerwinski F, Richardson AC, Oddershede LB. Quantifying noise in optical tweezers by allan variance. Optics express. 2009; 17:13255–13269. [PubMed: 19654731]
48. Norrelykke SF, Flyvbjerg H. Power spectrum analysis with least-squares fitting: amplitude bias and its elimination, with application to optical tweezers and atomic force microscope cantilevers. The Review of scientific instruments. 2010; 81:075103.doi: 10.1063/1.3455217 [PubMed: 20687755]
49. Killick R, Fearnhead P, Eckley IA. Optimal Detection of Changepoints With a Linear Computational Cost. J Am Stat Assoc. 2012; 107:1590–1598. DOI: 10.1080/01621459.2012.737745
50. Ribezzi-Crivellari M, Ritort F. Force spectroscopy with dual-trap optical tweezers: molecular stiffness measurements and coupled fluctuations analysis. Biophysical journal. 2012; 103:1919–1928. [PubMed: 23199920]
51. Marko JF, Siggia ED. Statistical mechanics of supercoiled DNA. Physical review. E, Statistical physics, plasmas, fluids, and related interdisciplinary topics. 1995; 52:2912–2938.
52. Ran FA, et al. Genome engineering using the CRISPR-Cas9 system. Nature protocols. 2013; 8:2281–2308. DOI: 10.1038/nprot.2013.143 [PubMed: 24157548]
53. Poser I, et al. BAC TransgeneOmics: a high-throughput method for exploration of protein function in mammals. Nature methods. 2008; 5:409–415. DOI: 10.1038/nmeth.1199 [PubMed: 18391959]

54. Kalaidzidis I, et al. APPL endosomes are not obligatory endocytic intermediates but act as stable cargo-sorting compartments. The Journal of cell biology. 2015; 211:123–144. DOI: 10.1083/jcb.201311117 [PubMed: 26459602]

55. Peplowska K, Markgraf DF, Ostrowicz CW, Bange G, Ungermann C. The CORVET tethering complex interacts with the yeast Rab5 homolog Vps21 and is involved in endo-lysosomal biogenesis. Developmental cell. 2007; 12:739–750. DOI: 10.1016/j.devcel.2007.03.006 [PubMed: 17488625]

56. Collinet C, et al. Systems survey of endocytosis by multiparametric image analysis. Nature. 2010; 464:243–249. DOI: 10.1038/nature08779 [PubMed: 20190736]

57. Gilleron J, et al. Image-based analysis of lipid nanoparticle-mediated siRNA delivery, intracellular trafficking and endosomal escape. Nature biotechnology. 2013; 31:638–646. DOI: 10.1038/nbt.2612

58. Takasato M, et al. Kidney organoids from human iPS cells contain multiple lineages and model human nephrogenesis. Nature. 2015; 526:564–568. DOI: 10.1038/nature15695 [PubMed: 26444236]

Europe PMC Funders Author Manuscripts

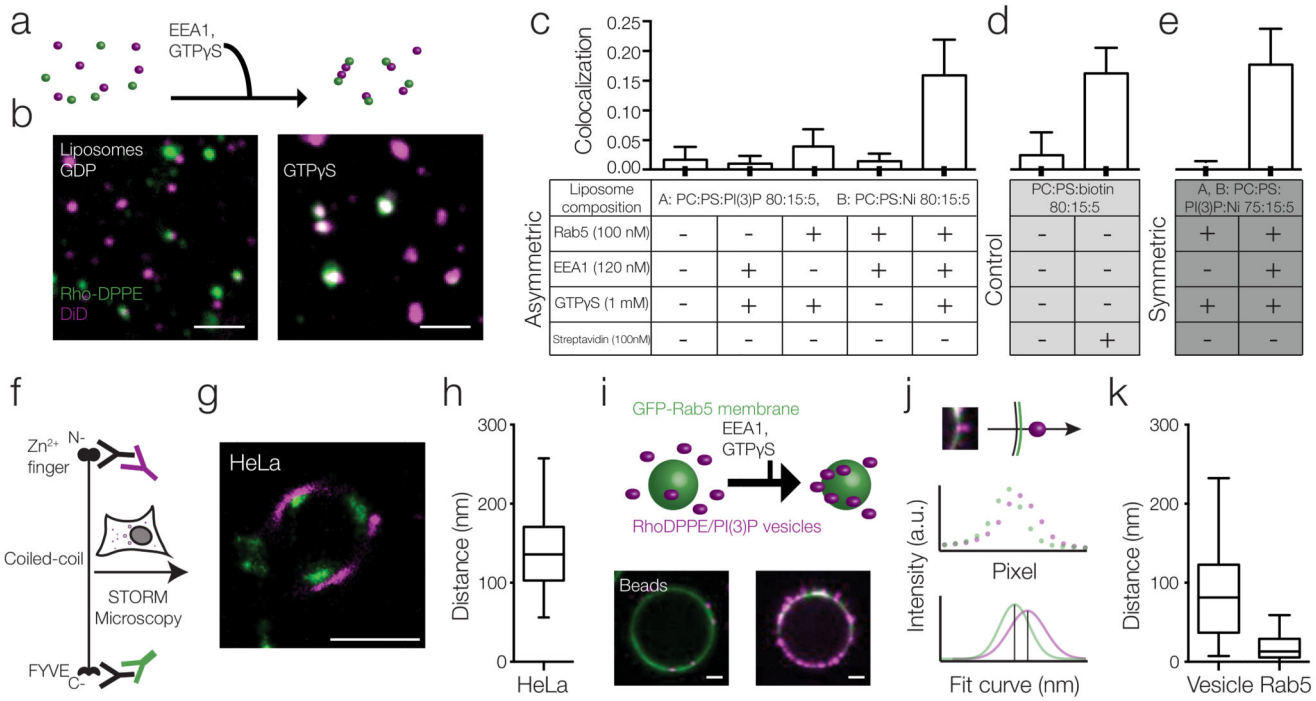

Figure 1. EEA1, Rab5, and PI(3)P form an asymmetric tethering machinery

a, b, Vesicle-vesicle tethering assay. Rho-DPPE liposomes harboring Rab5 (green) tether to DiD-PI(3)P liposomes (magenta) upon addition of EEA1 and GTPγS but not GDP (a, scheme, b, microscopy; representative of n=20). Scale bar 2 μm.

c-e Analysis of vesicle colocalization. Asymmetric (c) and symmetric (e) tethering required Rab5, PI(3)P and EEA1, Streptavidin-biotin control (d). (mean±s.d., n=3).

f-h *In vivo* STORM microscopy defines the extension of EEA1. The N-terminal (magenta) and C-terminal (green) domains of EEA1 (f) were differentially labeled. Representative STORM image (g, of n=22) and quantification of EEA1 extension (h, box-whisker with min/max error bars, n=86, representative experiment) from endosomes. Scale bar 500 nm.

i, Bead-supported membrane tethering similar to (a,b). Representative of n=20. Scale bar 2 μm.

j,k Distance of tethered vesicles (magenta) from the membrane (green). The intensity per pixel was plotted, fit to determine the relative distances, and quantified (k) (vesicle-membrane and Rab5-membrane, representative experiment; mean±s.d., n=36 and 14).

Europe PMC Funders Author Manuscripts

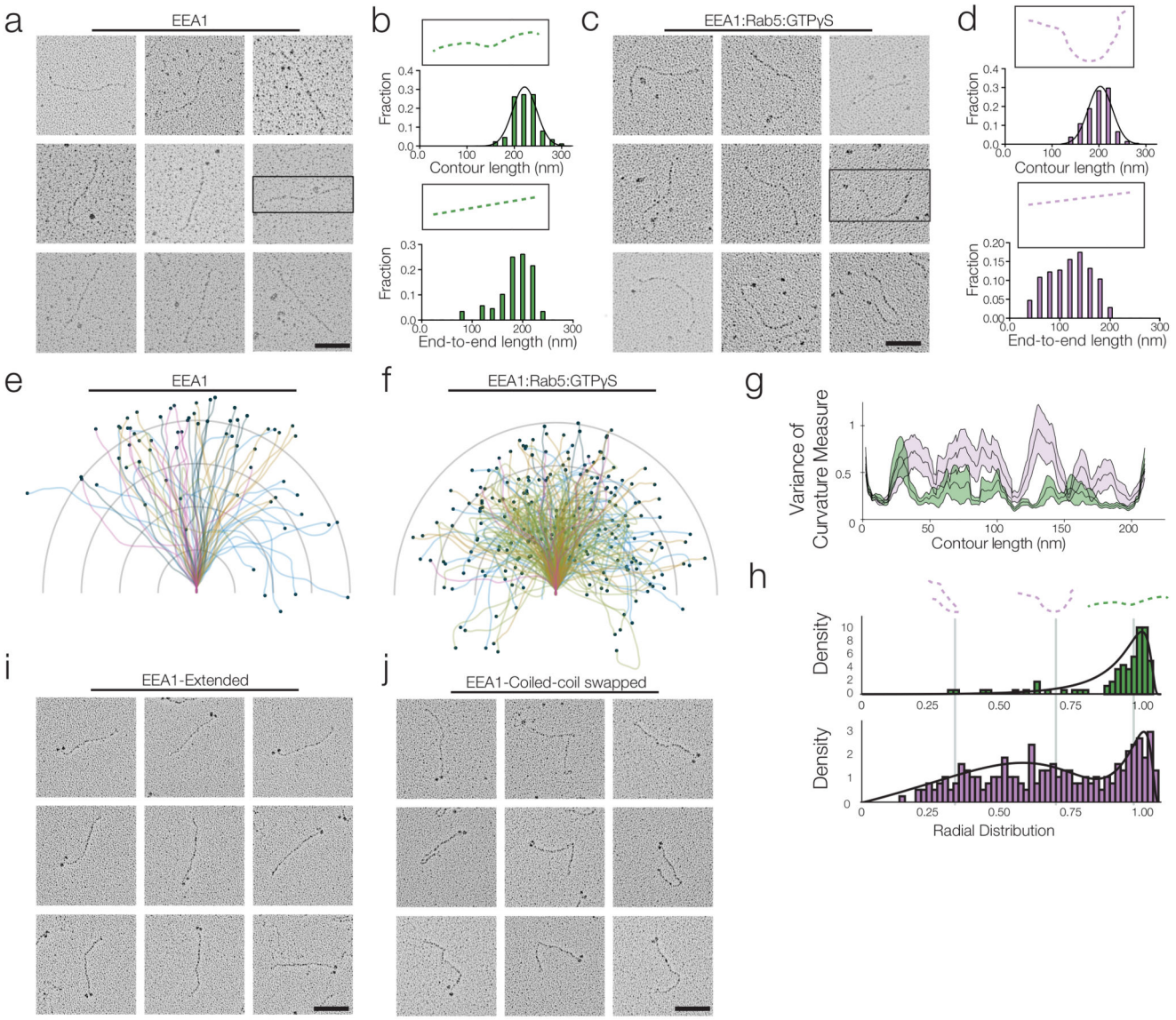

Figure 2. EEA1 changes flexibility upon Rab5 binding

a,c,i,j Representative examples of rotary-shadowing EM of EEA1 (a), EEA1+Rab5:GTPγS (c), EEA1-Extended and -Swapped variants. Scale bar 100 nm. *n*=88, *n*=212, *n*=90, *n*=145) respectively

b,d Contour and end-to-end length histograms for EEA1 (green, *n*=88), and EEA1+Rab5:GTPγS (magenta, *n*=212).

e,f Visual comparison of aligned EEA1 proteins. The highlighted ends of EEA1+Rab5:GTPγS lie significantly closer to the origin. Hemispheres demarcate 50 nm.

g, Variance of curvature measures along the contour of aligned EEA1+Rab5:GDP (green) and EEA1+Rab5:GTPγS (magenta) molecules. (*n*=90, *n*=145, respectively).

h, Radial distribution functions define the extension probability for EEA1±Rab5:GTPγS (-Rab5:GTPγS, green; +Rab5:GTPγS, magenta) with fit (black lines).

Europe PMC Funders Author Manuscripts

Europe PMC Funders Author Manuscripts

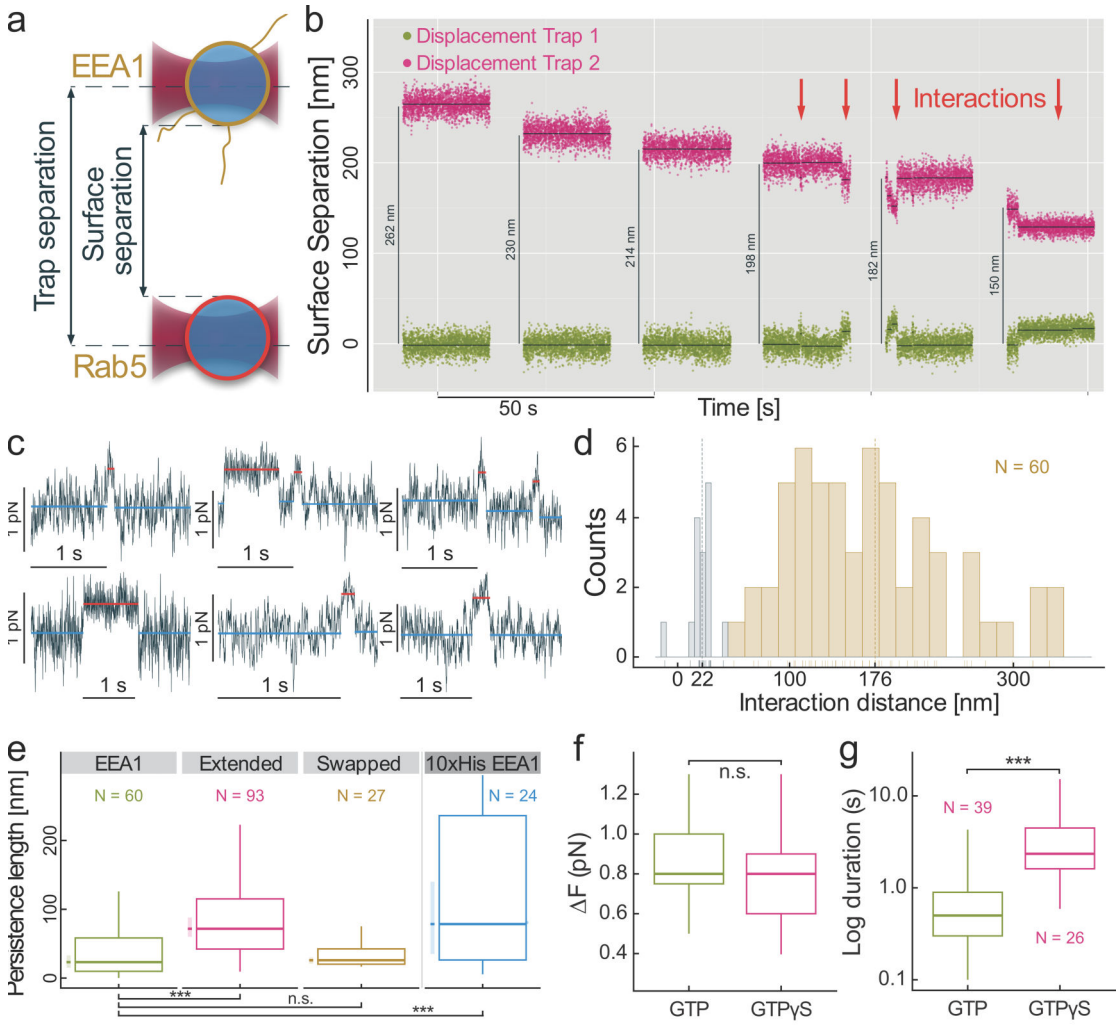

Figure 3. EEA1 collapse generates a force.

a, Scheme of bead-supported membranes harboring EAA1 or Rab5 captured by dual-trap optical tweezers.

b, c Traps moved successively closer until interactions (arrows) were observed, characterized by increase in force and decrease in variance (c).

d, Interaction distance consistent with length of extended EEA1. Silica microspheres (negative control) in grey.

e, Persistence length distributions of EEA1 and variants from optical tweezers measurements.

f, Force did not depend on GTP hydrolysis ($p>0.15$). n=39, 26 respectively.

g, Interaction duration was prolonged by GTPγS, $p<1e\text{-}4$. Mann-Whitney-Wilcoxon test, e-g. Box-whisker with Tukey error bars, e-g.

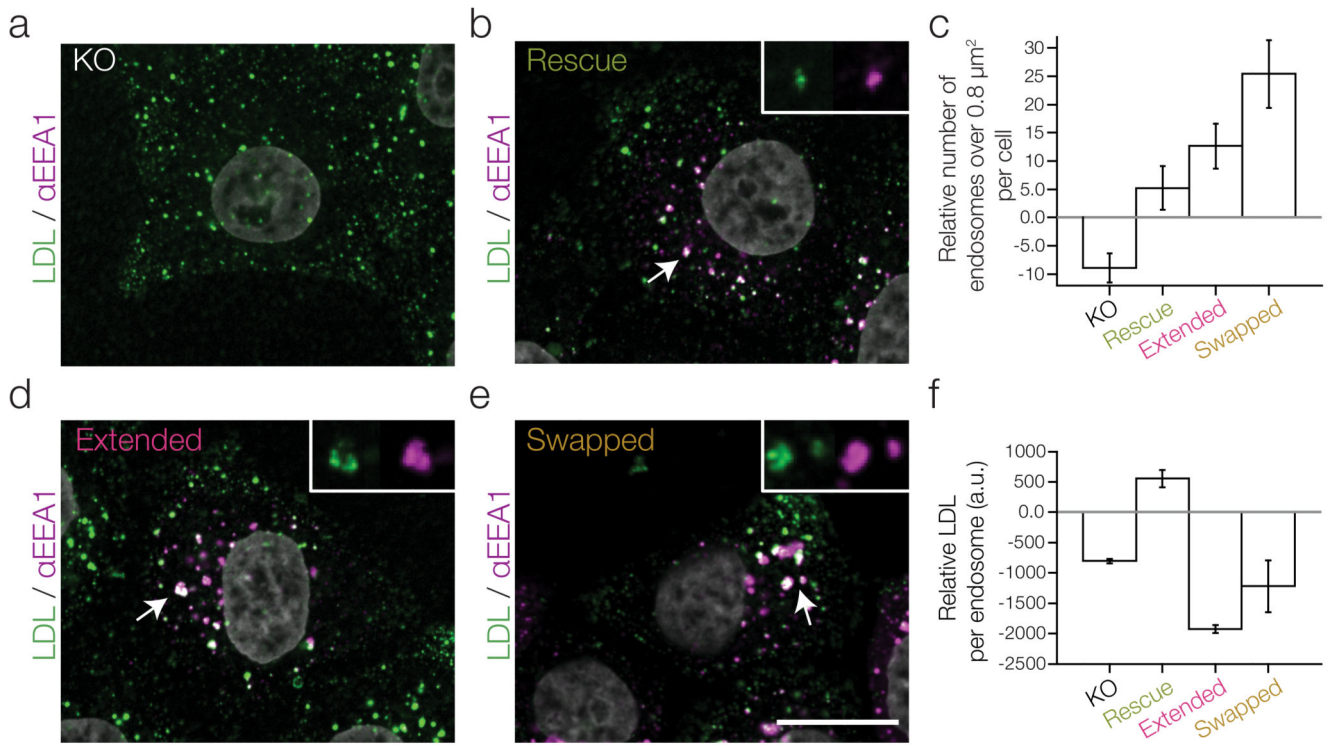

Figure 4. EEA1 mutants blocking entropic collapse induce trafficking defects.

a,b,d,e Confocal images of HeLa EEA1-KO cells (a), rescued with EEA1, Extended or Swapped mutants (b, d, e). Uptake of LDL (green) and immunostaining for EEA1 (magenta). Inset, endosomes depicted at arrows. Representative of n=30 images per condition (Methods). Scale bar 10 μm.

c, f Relative difference in number of large endosomes c), and LDL fluorescence (f). Mean ±s.d., representative experiment of 3, n=30 images. $p<0.01$ vs. HeLa, t-test, except Rescue.

Europe PMC Funders Author Manuscripts

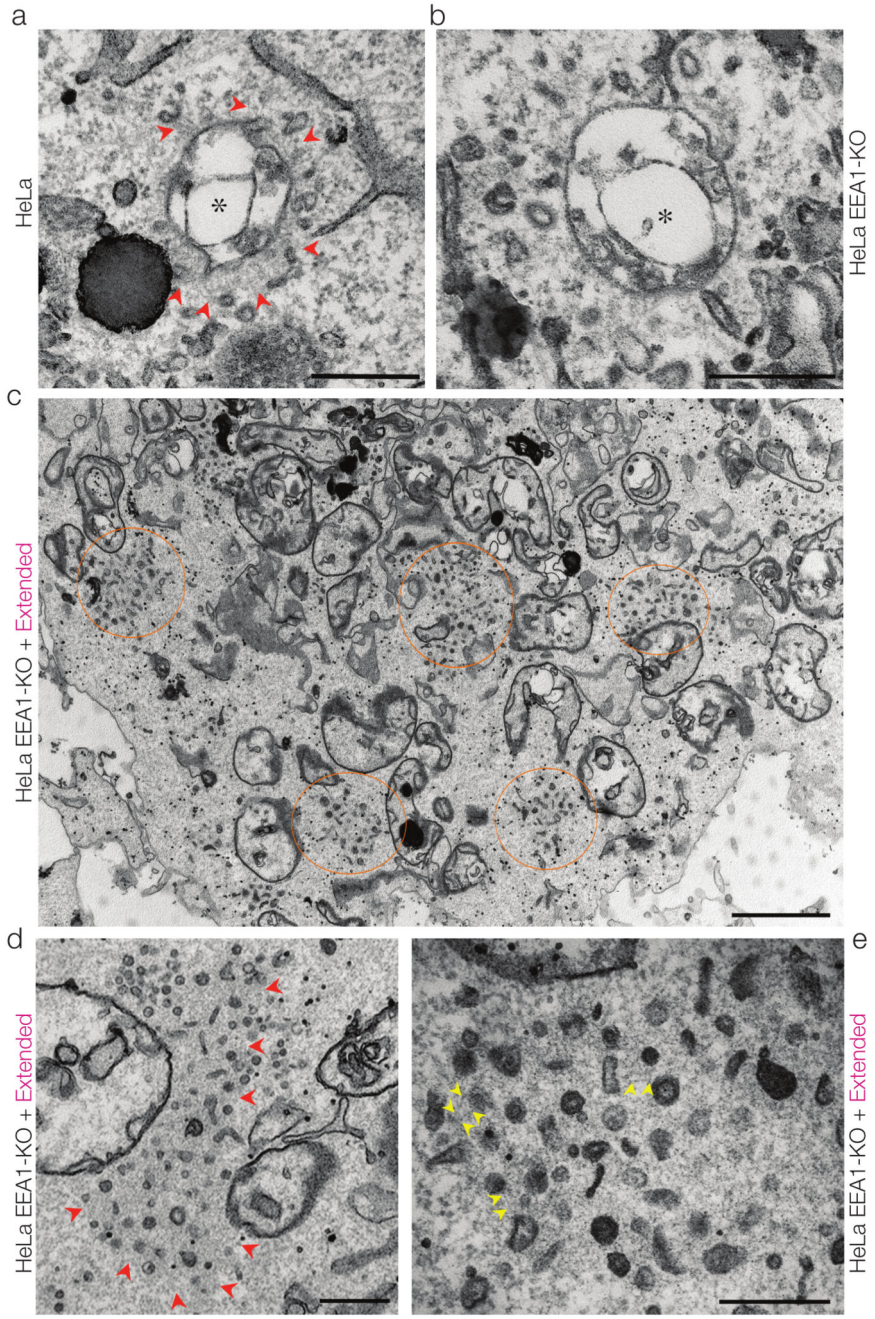

Figure 5. Ultrastructural analysis of EEA1 KO and mutant rescue cells.

a, Dense filamentous network (arrowheads) around an early endosome (asterisks) in HeLa. Many smaller vesicular or tubular profiles were consistently observed at the network periphery. Representative of n=33.

b, A filamentous network was less prominent in HeLa EEA1-KO with no obvious concentration of vesicles near the endosomal surface. Representative of n=54.

c-e, HeLa EEA1-KO expressing the Extended EEA1 variant showed clusters of vesicles throughout the cytoplasm and no classical endosomal morphology. The clusters were clearly

delineated by a zone of cytoplasm with distinct density (circled areas). Higher magnification revealed fine wispy material surrounding the clustered vesicles (d,e; arrowheads) and evidence of discrete filaments (between the arrowheads in e). Representative of n=56. Scale bars; panels a,b,d,e, 500 nm; c, 2 μm.

Europe PMC Funders Author Manuscripts